國立交通大學

電子物理研究所

博士論文

氮化銦鎵奈米結構之結構與光學特性

Structural and Optical Properties of InGaN Nanostructures

研究生：蔡仪哲 撰
指導教授：張文豪 博士

中華民國一百零一年七月

氮化銦鎵奈米結構之結構與光學特性

Structural and Optical Properties of InGaN Nanostructures

研 究 生：蔡仪哲　　Student: Wen-Che Tsai
指導教授：張文豪 博士　　Advisor: Dr. Wen-Hao Chang

國立交通大學
電子物理研究所
博士論文

A Thesis Submitted to
Institute of Electrophysics College of Science
National Chiao Tung University
in partial Fulfillment of the Requirements
for the Degree of
Doctor of Philosophy
in
Electrophysics July 2012
Hsinchu, Taiwan, Republic of China

中華民國一百零一年七月

氮化銦鎵奈米結構之結構與光學特性

研究生：蔡仪哲　　　　　　指導教授：張文豪 博士

國立交通大學電子物理研究所

中文摘要

本論文旨在探討氮化銦鎵奈米結構之結構與光學特性，其主要研究內容涵蓋兩個主題。首先，在論文的第一部份，我們針對氮化銦鎵奈米結構，進行應變釋放及成核過程的研究。其中，我們利用拉曼光譜，針對不同大小且未覆蓋的氮化銦島狀物進行應變釋放的研究。實驗結果指出不管透過何種方式所成長的氮化銦島狀物，其拉曼譜線的峰值將隨著高寬比的增加而紅移。另外，我們也探討存在於氮化銦與氮化鎵介面中的初始壓應變量，發現此應變量在島狀物剛形成時便透過塑性鬆弛的方式進行釋放，且其釋放程度高達 96 % 以上。而殘餘約 -3.5×10^{-3} 的應變量將隨著島狀物的成長再以彈性鬆弛的方式進行釋放。最後根據簡化之 2-D 模型分析及 3D 模擬結果，建立氮化銦島狀物應變釋放的過程與大小及形貌之間的關係。此外，我們也利用有機金屬氣相磊晶系統，透過成長溫度的改變 (550-750 ℃) 成長高銦組成的氮化銦鎵奈米點，並探討其表面形貌、合晶的組成及螢光光譜特性。我們觀察到氮化銦鎵奈米點的成核過程主要是由銦原子所主導。其中，鎵原子溶入氮化銦的過程主要是由原子的遷移能力所決定。因此當氮化銦鎵成長於較高的溫度時，傾向於分別形成高銦組成的島狀結構與高鎵組成的薄膜。其中高銦組成的島狀結構其螢光訊號位於近紅外區域，而高鎵組成的薄膜則被認為是可

見光訊號的主要來源。在討論完氮化銦島狀物在成長初期時應變釋放的過程後，我們也研究氮化銦鎵薄膜，在不同銦組成下 (0.13<x<0.38) 其應變釋放的情況。並透過高解析度x光繞射儀及倒置空間圖，進而探討薄膜中，應變釋放所導致銦含量分佈不均勻的特性。根據結構上的分析，我們發現在螢光光譜上所觀察到的雙螢光譜峰與氮化銦鎵的應變釋放情況有關。此外，我們更利用變溫及時間解析螢光光譜進一步分析此雙螢光譜峰，並透過螢光強度隨溫度的變化及載子動態的討論，進而了解其光學特性。最後，我們歸納出氮化銦鎵薄膜中，發光效率與侷限態效應相關的特性。

在論文的第二部分，我們利用顯微螢光光譜技術，量測奈米線寬度介於 9-27 奈米的單根氮化銦鎵/氮化鎵奈米線。在低溫環境下，我們可觀察到氮化銦鎵中來自於侷域化激子複合所產生的單一譜線。透過能量隨激發功率的變化，譜線隨時間飄移的情況，及時間解析螢光光譜，我們發現極化場在氮化銦鎵/氮化鎵異質結構中並不顯著。最後經由組成的分析及有限元素法的模擬，我們猜測銦-鎵原子在介面的擴散情況將對氮化銦鎵/氮化鎵異質結構的應力釋放有所影響。此外，我們也透過壓電材料，討論氮化銦鎵/氮化鎵奈米線中，能隙隨外加應力調變的情況。實驗結果指出，螢光譜峰的能量將隨外加壓應力而藍移。根據數值模擬的結果，發現到所外加的雙軸應力將產生一沿著奈米線之非等向性的應變。由於在我們研究的奈米線中，並無內建壓電場及量子侷限效應，因此實驗所觀察的螢光譜峰位移可歸納於應變所導致的能隙變化量。

Structural and Optical Properties of InGaN Nanostructures

Student: Wen-Che Tsai　　　　　Advisor: Wen-Hao Chang

Institute of Electrophysics National Chiao Tung University

Abstract

The dissertation is devoted to the structural and optical properties of InGaN nanostructures. The main focus of this dissertation can be divided into two parts. First, strain relaxation and nucleation process of $In_xGa_{1-x}N$ nanostructures grown by MOCVD are comprehensively studied. The Raman spectroscopy has been utilized to study the strain relaxation in uncapped InN/GaN islands of different sizes. A redshift in the Raman peak with the island's aspect ratio was observed, regardless of how the InN islands were grown. Most of the initial compressive strain at the InN-GaN interface was found to be released plastically, with a relaxation degree up to > 96 %, during the initial stage of island formations. After that, the residual strain of only -3.5×10^{-3}, was further relaxed elastically via the surface islanding. Based on a simplified 2D model analysis and full 3D simulations, we established the relationship of the strain relaxation in InN/GaN islands with their size and shape. Besides, the surface morphologies, alloy compositions and PL properties of In-rich InGaN nanodots grown

by MOCVD at $T_g = 550\text{-}750$ °C have also been investigated. The nucleation of InGaN dots was found to be dominated by the surface migration of In adatoms. In particular, we found that the incorporation of Ga into InN during the growth of InGaN dots is governed by adatom migration capability, which tends to decompose into In-rich islands and a thin Ga-rich layer at higher growth temperatures. In-rich islands exhibit PL emission in the NIR range, while the formation of a thin Ga-rich layer is likely to be responsible for the observed visible emission band. After discussing the strain relaxation of InN islands during the initial stage, the strain relaxation in thick $In_xGa_{1-x}N$ films with x ranging from 0.13 to 0.38 are also discussed. The In composition inhomogeneity accompanied by strain relaxations in the InGaN films are studied by high-resolution x-ray diffractions (XRD) and reciprocal space mapping (RSM) along an asymmetric axis. According to the structural analysis, the observed double PL peaks are associated with the strain relaxation in the InGaN films. Besides, further studies on double peaks are also performed by temperature dependent and time-resolved PL. The optical characterizations such as integrated PL intensities versus temperatures and carrier dynamics are demonstrated clearly. Finally, the correlation between emission efficiency and localization effect in InGaN film is also concluded.

In the second part of the dissertation, we present microphotoluminescence (μPL) measurements on single InGaN/GaN NWs with diameters in the range of 9-27 nm. Sharp emission lines originated from the recombination of localized excitons in the InGaN layers can be resolved at low temperatures. Excitation dependent energy shifts, spectral diffusions, time-resolved PL measurements of these emission lines indicate that the polarization field is insignificant in the InGaN/GaN heterostructures. Composition analyses together with FEM simulations suggest that In-Ga intermixing also play a role in the strain relaxations in InGaN/GaN NW heterostructures. Besides, we also demonstrate the band-gap tuning of InGaN/GaN NW heterostructures in the part by applying an external stress using a piezoelectric actuator. The luminescence peak energy of InGaN/GaN NWs shows blueshift with the applied compressive stress. According to numerical simulations, applying a biaxial stress will induce an anisotropic strain along the NW. Due to the lack of internal electric field and quantum confinement effect in NW heterostructures, the shift in the PL peak energy can be attributed to the strain induced change in the energy gap.

誌謝

八年的交大生涯在隨著誌謝的撰寫下總算告一段落。回首這些年來，除了專業領域上的成長外，在面對問題時心態上的轉變及成熟更是這些年來最重要的收穫。雖然這過程苦樂參半，然而我卻感謝這一切的發生，感謝這歷程中陪我走過的每一個人，因為這些都將成為我永難忘懷的回憶。

衷心感謝我的指導教授 張文豪博士，不論是在研究或是在為人處事上，老師總是在我面前樹立了良好的楷模供我學習與成長。在研究上，老師嚴謹與執著的態度，讓我了解到治學與做事應有的認真與嚴肅的態度。此外老師在面對問題時從容不迫的態度，針對問題的根本尋求對策，並進而有效率的解決問題，更是讓我多所省思，獲益良多。而我深信這些年下來的學習與成長，將對於我日後的發展有著深遠的意義與影響。另外，我要感謝我的另一個指導教授 李明知博士。初期的博士班求學過程中，我總是不夠成熟的處理著實驗室的事情，但老師總是給予我一次又一次的機會去學習與證明自己，即便後來老師退休了，但我還是能體會到老師對我的關懷與照顧。師恩浩瀚無以言謝，希望帶著從老師身上學習到的種種，在日後走出屬於自己的一片天空，不辜負老師們的期許與教導。

感謝周武清教授這些年來的指導與鼓勵，尤其是在我遇到生活上的問題時，老師毫不遲疑地伸出援手，給予我最需要的協助與幫忙，點點滴滴學生銘感於心。特別感謝陳衛國教授、台大凝態中心的林麗瓊教授及其所領導的磊晶研究群，若沒有他們所提供的半導體樣品，這篇論文是無法順利完成的。還要感謝口試委員們的指導，包括中央徐子民教授、清大果尚志教授，謝謝委員們對我論文內的指導、建議與鼓勵，使我獲益匪淺，在此亦表達個人內心最深的感謝。

這一段多采多姿的生活，幸賴許多學長與學弟妹們的陪伴與協助，讓我得以度過挫折與困難。感謝古慶順博士在我剛接觸半導體光學時的引導與協助，奠定了日後許多光學量測的概念與基礎;感謝張富欽博士、柯文政博士、李寧博士及陳京玉博士，在這一路上給我的提攜與幫助。感謝博士班學弟妹林萱、少甫、昱安、家賢、瑋廷、衍均在這

幾年給予我在研究上、精神上及生活上的幫助，使得我在研究這條路上並不孤單；感謝這八年來一起打拼的學弟妹們碧軒、啟仁、士傑、峰毅、聖允、威宇、家和、詠盛，因為你們的貢獻與參與，我才能順利完成這篇論文。另外我還要感謝這些年來陪伴我同甘共苦的學弟妹們，包括士凱、書鴻、士興、阿龐、志豪、小周、國榮、峰菖、健家、韋辰、若榕，因為你們的存在，使得博士班的生活不再那麼枯燥，謝謝你們。謝謝我的學妹詩涵，最後這一年因為你的支持與鼓勵，使得我有力量完成並拿到這得來不易的學位。總之，該感謝的人真的很多。未被提及的師長及同伴們，請見諒，並容我在此一起誌謝。

最需要感謝的還有我的父母及弟妹，謝謝你們全力的支持與包容，讓我能在求學路上心無旁鶩地持續邁進。另外我還要感謝心怡，很感謝你這些年來的鼓勵與支持，不管未來如何，真的很謝謝你在這些年對我的付出與關心。同時我也要感謝神讓我在徬徨無助時仍能找到力量完成這條屬神的道路。

最後僅以這篇論文獻給我的家人，謝謝你們。

蔡佼哲　於工程六館

中華民國一百零一年七月三十號

CONTENTS

LIST OF TABLES

LIST OF FIGURES

Chapter 1 General Introduction

1.1 Foreword

In 1994, Nakamura *et al*. reported the first blue light-emitting diode (LED), which was made from a InGaN/GaN heterostructure exceeding 1cd in brightness [1]. Then blue/green InGaN single quantum well (SQW) structures LEDs are also developed in 1995 [2]. Besides the development in LEDs, the room temperature (RT) violet laser light emission in InGaN/GaN/AlGaN-based heterostructures under pulsed and continuous-wave (cw) operations were also achieved [3-5]. In 2002, the InGaN-based materials are even proposed to fabricate high efficiency white light emitters which are predicted to play an important role in future lighting system [6] by combining UV-emitting GaN LEDs with phosphors.

As we know, the InGaN active layers in LEDs and LDs include a large number of threading dislocations (10^9-10^{10} cm^{-2}), that originate from the interface between GaN and the sapphire substrate due to the large lattice mismatch ($\Delta a/a = 16\%$). However, in spite of the large number of dislocations, the efficiency of the InGaN-based LEDs and LDs is much greater than that of the conventional compound semiconductor (AlGaAs and AlGaInP)-based LEDs and LDs. To interpret the defect-insensitive emission probability in InGaN, more research efforts have been made and numerous models have been proposed by many research groups. In 1996, Chichibu *et al.* assigned the electroluminescence (EL) peak in InGaN QW

LEDs to the recombination of excitons localized at potential minima originating from InN-rich lower bandgap regions [7]. This kind of random localization of excitons was proposed to prohibit nanradiative recombination of the excitons at threading dislocations. In 1997, the presence of In-rich InGaN [8,9] or pure InN quantum dot [10] within InGaN QW was found to be the localization centers through transmission electron micrograph (TEM) observations [8,9]. However, the detailed TEM studies have indicated that such dotlike structures may be artifacts due to radiation damage during TEM observation in 2004 [11]. Furthermore, compositional or strain inhomogeneity [12] was also proposed as the origin of exciton localization and it has often been correlated with defect-originated microstructures [13].

In addition to defect, a c-plane LED composed of strained InGaN QWs has another disadvantage, namely the quantum confined stark effect (QCSE) caused by the polarization induced electrostatic fields [14]. Generally, the resulting piezoelectric field will cause the redshifted emission energies and the lower in overlap of electrons and holes wavefunction [15-16]. However, InGaN based LEDs still exhibit the high emission efficiency despite the presence of above disadvantages.

Few years ago, many reports state the value of 0.65-0.9 eV for the energy gap of InN instead of the previously accepted values 1.9 eV [17-21]. This finding has stimulated considerable interest, since the potential application of ternary $In_xGa_{1-x}N$ alloys can be further extended into the near infrared (NIR) range. For instance, it provides an almost perfect match with the complete solar spectrum, which makes InGaN a potential material for high efficiency multijunction solar cells [22].

Besides the researches on thin film growth, the $In_xGa_{1-x}N$ nanostructures such as quantum dots and nanowires have also been under extensive investigations due to their fascinating properties. For instance, the InGaN LD could improve their performance enormously by introducing self-assembled InGaN quantum dots (QDs) into device active layers. Higher brightness, lower threshold currents [23], and better temperature stability [24] could result. In addition, the one dimensional (1D) nanostructures are unique because they exhibit discrete density of states and at the same time maintain continuous transport path. A various 1D nanostructures of GaN and InN, such as, nanorods, nanowires, nanobelts and nanotubes, have also been synthesized successfully [25,26].

However, if we attempts to use the $In_xGa_{1-x}N$ nanostructure as an element of the next generation devices, more understanding of the structural and optical properties of $In_xGa_{1-x}N$ nanostructures are needed. Recently, with the progress of studying the $In_xGa_{1-x}N$ nanostructures at National Chiao Tung University, we investigate and understand the many properties existed in $In_xGa_{1-x}N$ nanostructures. We have employed several spectroscopy characterization techniques to study the nanostructures, including X-ray diffraction (XRD), atomic force measurement (AFM), photoluminescence (PL) and Raman scattering. In this thesis, we will present the physical characteristics of the InGaN nanostructures in many respects, based on our recent investigations regarding their structural and optical properties. Many phenomena involved in the thesis have been discussed and understood, but some of them still need further studies. However, we believed that the applications of InGaN nanostructures can be developed progressing in the next few years, if the more structural and optical properties of them can be further understood.

1.2 Outline

The contents of the thesis surround the structural and optical properties of $In_xGa_{1-x}N$ nanostructures. Before discussing the structural and optical properties, a theoretical background is presented firstly in Chapter 2 to understand the fundamental physics happened in the $In_xGa_{1-x}N$ alloys. A brief review of recent advances in the growth of $In_xGa_{1-x}N$ alloys by MBE and MOCVD is presented in Sec. 2.1. The relationship between In composition and emission wavelength is also demonstrated. The strain effects on InN studied by Raman scattering are discussed in Sec. 2.2. The reported strain-free Raman frequencies of E_2 mode are reviewed briefly in the section. Besides, the estimation of residual strain through frequency shift of E_2 mode and phonon deformation potential is also demonstrated. At the end of Chapter 2, we discuss the strain effect on III-nitrides. The bandgap and piezoelectric polarization after strain modification is presented. Since the strain play an important role on the electronic and optical properties, the discussions in this section can provide the further understanding of inherent properties in III-nitrides.

The main focus of Chapter 3 is the structural and optical properties of InGaN nanostructures grown by MOCVD. In Sec. 3.2, we present the strain state of InN islands by Raman scattering measurements. Size dependent strain relaxation in InN islands is comprehensively discussed. Besides, the general features of In-rich InGaN islands such as surface morphology, alloy composition and PL spectrum are also discussed in the section. In

Sec. 3.3, we employed the reciprocal space mapping (RSM) to study the strain and composition distribution in Ga-rich InGaN films. Optical properties of strained and relaxed phase existed in InGaN films are clarified in this study.

In Chapter 4, we present the unique characterizations of 1-D InGaN/GaN nanowires grown by MBE. In Sec. 4.2, optical properties of single InGaN/GaN nanowires with thin diameter are investigated. The suppression of piezoelectric field in a single nanowire is also evident from the optical spectroscopy investigations. After discussing the general features of InGaN/GaN nanowires, we demonstrated the bandgap tuning of nanowires by applying an external stress using a piezoelectric actuator. The luminescence peak energy as a function of the applied stress is investigated and also compared with the theoretical prediction from COMSOL simulation package.

Finally, we summarized the conclusions of these studies in Chapter 5.

Chapter 2 Theoretical Background

2.1 Brief overview of $In_xGa_{1-x}N$ growth

In the past decade, considerable efforts have been devoted to the growth of $In_xGa_{1-x}N$ alloys in the entire composition range using both MOCVD and MBE. However, the growth of high quality In-rich InGaN layer remains challenging due to the low solubility of InN in GaN which has been theoretically predicted and experimentally observed in the late 1990s [27-29]. In 1998, Karpov *et al.* proposed that phase separation can be suppressed during the epitaxial growth of strained InGaN film [30]. The calculation indicated that a lower critical temperature (750 ^{o}C) and increased solubility (35 %) can be achieved for strained InGaN alloy. The result has been further evident by Tabata *et al.* in 2002 [31], where the phase separation induced by spinodal decomposition in InGaN layers can be suppressed by biaxial strain according to Raman measurements.

Besides, controlling the growth temperature has also been proposed to suppress the phase separation effect. In 1999, single phase $In_xGa_{1-x}N$ films ($0.5<x<1$) has been grown successfully by MOCVD using a lower growth temperature down to 550 ^{o}C [32]. More recently, InGaN alloys including nanowires without phase separation have been grown by MBE or low pressure halide phase epitaxy with the entire composition range [33,34]. In this section, a brief review of recent advances in the growth of $In_xGa_{1-x}N$ alloys by MBE and

MOCVD is presented. The relationship between In compositions and emission wavelengths will also be discussed and demonstrated.

In 2002, a first set of $In_xGa_{1-x}N$ alloys ($0.36<x<1$) was successfully grown by MBE [35]. From X-ray, PL, and Raman measurements, the $In_xGa_{1-x}N$ alloys were found to exhibit only a hexagonal structure without phase separation. Also in 2002, high quality In-rich InxGa1-xN films ($0.5<x<1$) have been grown on sapphire substrate by MBE [36]. They demonstrated that InN has narrow bandgap energy of 0.77 eV at room temperature and that the bandgap increases with increasing Ga content. A similar finding has also been reported by Nanishi et al. in 2003 [37], where the fundamental bandgap of InN is found to be 0.8 eV at room temperature. Besides, InGaN films with an entire alloy composition were grown at low temperature (550 ^{o}C) without noticeable phase separation. Based on the above results, we can find that the single phase and entire alloy composition of InGaN alloys can be successfully grown by MBE. This breakthrough can be attributed to the efficient atomic nitrogen species for incorporation into the growing front, which is independent of the substrate temperature in MBE system [38]. This advantage facilitates the growth of In-rich InGaN alloys at lower growth temperatures without phase separation.

On the contrary, the progress in MOCVD growth of In-rich InGaN alloys is relatively slower. Chang *et al.* reported that single crystalline $In_xGa_{1-x}N$ films ($0.7<x<1$) can be grown by MOCVD [39]. However, two PL peaks were observed for $In_{0.8}Ga_{0.2}N$, indicative of the presence of phase separation in the InGaN alloy. In 2008, single phase $In_xGa_{1-x}N$ alloys ($0.25<x<0.63$) have been grown successfully by MOCVD [40]. They suggested that the presence of strain and low growth temperature (610-730 °C) have promoted the suppression of phase separation. However, further improvements in the material quality are still necessary for the development of InGaN-based devices.

Tab. 2.1: InGaN alloys grown by MBE and MOCVD.

	Method	Growth temp (°C)	Composition
W. J. Schaff and J. Wu	MBE	470-570	$0.5<x<1$
Nanishi *et al.*	MBE	500-550	$0<x<1$
Mamutin and Davydov	MBE	350-500	$0.36<x<1$
Chin-An Chang and Nie-Chuan Chen	MOCVD	550-900	$0<x<1$ (p-type)
H. X. Jiang	MOCVD	610-730	$0.25<x<0.63$
Euijoon Yoon	MOCVD	640-800	$0<x<1$

The relationship between In compositions and emission wavelengths is shown in Fig. 2.1. It clearly indicated that InGaN alloys with emission wavelength covering from near-ultraviolet to the near infrared range have been realized by MBE. On the contrary, only the Ga-rich (x<0.3) and In-rich (x>0.8) InGaN alloys with emission wavelengths below 600 nm and beyond 1200 nm have been achieved by MOCVD growth.

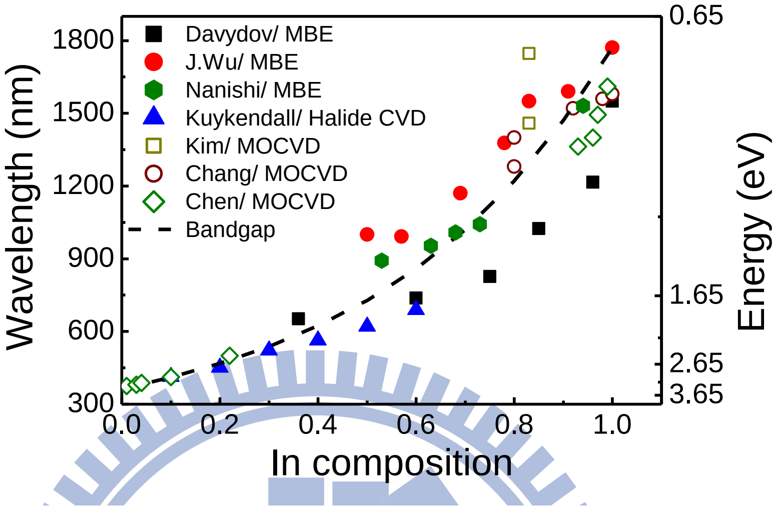

Fig. 2.1: Emission wavelength versus In composition of $In_xGa_{1-x}N$ alloys.

2.2 Strain effects on InN studied by Raman Scattering

Since the strain can influence growth behaviors and optical properties of III-nitrides, it is important to discuss and understand the strain status in the heterostructures. Raman scattering is a nondestructive, contactless and efficient method to measure the strain exhibited in heterostructures. In the section, we will introduce how to determine the strain state in InN films by Raman measurements. Some experimental results of strain-free Raman frequencies and deformation potentials will be illustrated, of which the commonly accepted values will be pointed out.

Wurtzite InN belongs to the space group C_{6v}^4. Group theory predicts that there are eight sets of phonon modes at the Γ points in the Brillouin Zone ($2A_1 + 2E_1 + 2B_1 + 2E_2$). The atomic displacement scheme of these optical modes is shown in Fig. 2.2. Among them, the E_2^H phonon mode is sensitive to the residual biaxial strain [41-43] due to the lattice displacement being parallel to the *a-b-plane*. In the following, the discussions will be limited to the strain-free Raman frequencies and the deformation potentials for the E_2^H mode.

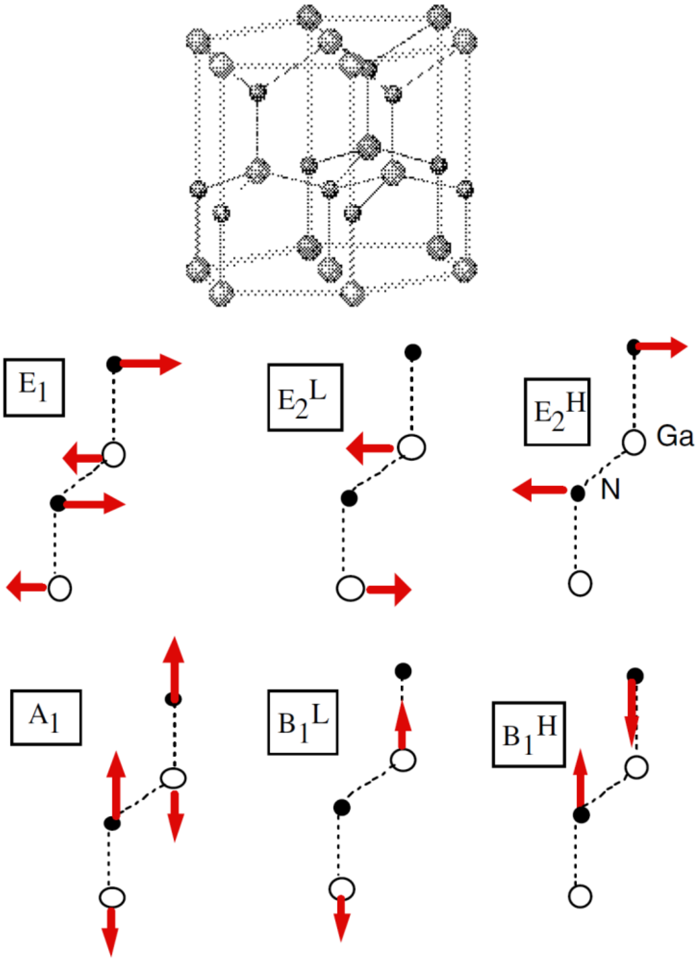

Fig. 2.2 : Optical phonon modes in the wurtzite structure. There are two types of the E_2- and B_1-type modes that are distinguished by superscripts L and H. [Reproduced from H. Harima, J. Phys. C **14**, R967 (2002)].

Table 2.2 shows the strain-free Raman frequency for the E_2^H modes of InN reported over the past few years (1996-2002). It can be seen that the frequency is quite scattered and the reported values are in the ranges of 483-495 cm^{-1} for the E_2^H mode.

Tab. 2.2: Raman E_2 mode frequency reported for hexagonal InN.

	E_2^H (cm^{-1})	Ref.
Experimental		
	495	44
	491	45
	488	46
	490	47
	489	18
Theoretical		
	483	46
	492	47

In 2006, InN films with a thickness of about 2.3 μm were grown at different temperatures by plasma-assisted molecular beam epitaxy (MBE) [48]. By combining the measured Raman frequencies and the residual strains obtained from reciprocal space mapping, the Raman frequency of E_2^H mode for strain-free InN was to be 489.8 cm^{-1}. The deduced value is also consistent with the values reported by Pinquier *et al.* (2004) and Chen *et al.* (2005) [49,50]. Therefore, in the thesis, we will adopt this experimental value to estimate the residual strain in InN islands from Raman frequency shifts.

The frequency shift of E_2 mode can be related to the strain by

$$\Delta\omega = 2a\varepsilon_a + b\varepsilon_c , \tag{2.1}$$

where a and b are deformation potentials, while ε_a and ε_c are the in-plane and out-of-plane strains in InN. Using $\varepsilon_c / \varepsilon_a = -2\nu/(1-\nu)$, and the reported Poisson ratio of $\nu = 0.21$ for InN epilayer [51], we can obtain

$$\Delta\omega = (2a - 0.53b)\varepsilon_a . \tag{2.2}$$

According to the simplified equation, the residual strain can then be calculated while the deformation potential is determined. Since the deformation potentials can be affected by the elastic stiffness constant values, we deduce the deformation potentials a_{E2} and b_{E2} as listed in Table 2.3 using the elastic stiffness constants from several different literatures.

Tab. 2.3: Elastic stiffness constants and deformation potentials for the E_2 mode of InN.

C_{11}	C_{12}	C_{13}	C_{33}	a_{E2} (cm^{-1})	b_{E2} (cm^{-1})	Ref.
190	104	121	182	-938	-407	52
223	115	92	224	-960	-489	53
271	124	94	200	-998	-635	54
204	85	72	217	-893	-236	55

As shown in Table 2.3, the uncertainty exists in the obtained deformation potentials arising from the different stiffness constants (C_{ij}). However, there are small deviations between values of the deformation potential a for E_2^H mode using different stiffness constants. This is meaningful because the deformation potential a is more important in determining the biaxial stresses in InN films from Raman measurements. Here, we adopt the value reported in Ref. 30 to calculate the deformation potential in the thesis. Because the values are smaller than AlN and close to the GaN, which is reasonable due to the weaker bonding in InN.

In summary, the residual strain can be estimated directly in III-nitride layers by Raman scattering according to the shift of phonon modes, while we obtain the strain-free Raman frequency and phonon deformation potential.

ESA 1896

2.3 Influence of strain effect on III-nitrides

2.3.1 Bandgap

Due to the large differences in lattice constants and thermal expansion coefficients between the substrate and the nitride layers with different alloy compositions, strain is always present in group-III-nitride epilayers. However, this residual strain will modify the bandstructure and electronic properties obviously. Therefore, in this section, we will brief introduce the bandstructure of wurtzite structure firstly. Then, the influence of strain on GaN and AlN bandgap energy will also be demonstrated.

In the wurtzite structures of GaN and AlN, the conduction band (C. B.) minimum and the valence band (V. B.) maximum are located at the Γ point in the Brillouin Zone (BZ), as shown schematically in Fig. 2.3. They are related to Γ_{1c}, Γ_{6v} and Γ_{1v} states without considering the spin-orbit interaction. Because the Γ_{6v} and Γ_{1v} states are separated by a crystal field splitting, two energy gaps can be defined by $E_{A/B} = E_{\Gamma_{1c}} - E_{\Gamma_{6v}}$ and $E_c = E_{\Gamma_{1c}} - E_{\Gamma_{1v}}$, according to the transitions $\Gamma_{6v} \rightarrow \Gamma_{1c}(A, B)$ and $\Gamma_{1v} \rightarrow \Gamma_{1c}(C)$. Among them, $E_{A/B}$ is the fundamental gap of GaN, whereas E_c is the transition gap of AlN due to the negative crystal field splitting.

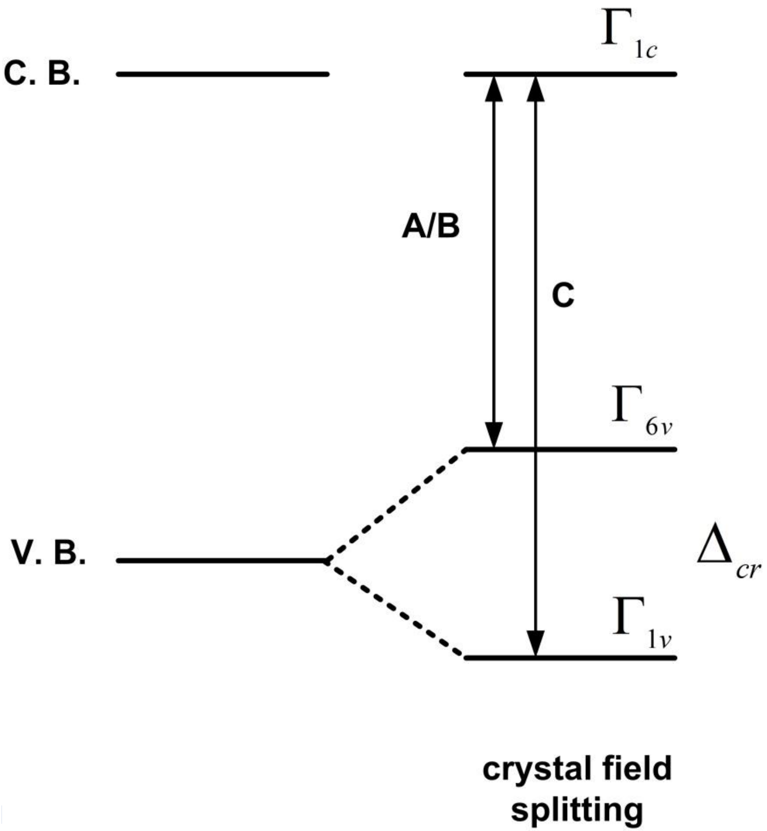

Fig. 2.3: Schematic diagram of wurtzite bandstructure.

Once the strain is present in the nitride layer, both the energy gap and crystal field splitting are modified, as illustrated in Fig. 2.4.

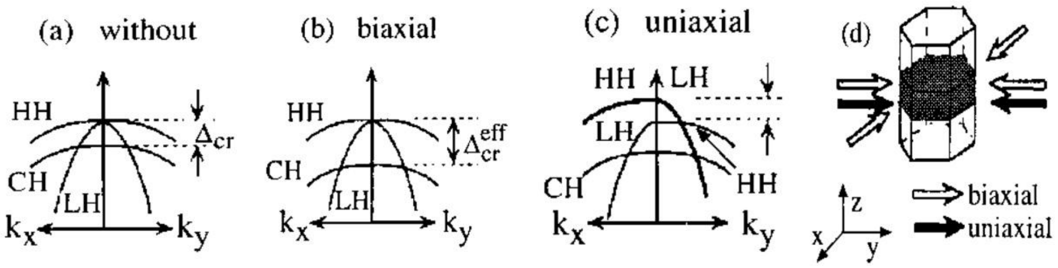

Fig. 2.4: Schematic band structure near the top of the valence bands of the WZ GaN in the k_x-k_y plane ; (a) without strain, (b) with a biaxial strain, and (c) with a uniaxial strain in the *c* plane. The direction of each strain is shown in (d). [Reproduced from M. Suzuki *et al.*, J. Appl. Phys. **80**, 6868 (1996)].

To determine the bandstructure with strain, the components of strain tensor and deformation potentials are required. Without considering the spin-orbit interaction, the three energy bands can be described as follows:

$$E_{\Gamma_{1c}}(\varepsilon)=E_{\Gamma_{1c}}(0)+a_{cz}\varepsilon_{zz}+a_{ct}(\varepsilon_{xx}+\varepsilon_{yy}), \tag{2.3}$$

$$E_{\Gamma_{6v}}(\varepsilon)=E_{\Gamma_{6v}}(0)+D_1\varepsilon_{zz}+D_2(\varepsilon_{xx}+\varepsilon_{yy})+D_3\varepsilon_{zz}+D_4(\varepsilon_{xx}+\varepsilon_{yy}), \tag{2.4}$$

$$E_{\Gamma_{1v}}(\varepsilon)=E_{\Gamma_{1v}}(0)+D_1\varepsilon_{zz}+D_2(\varepsilon_{xx}+\varepsilon_{yy}), \tag{2.5}$$

where a_{cz}, a_{ct}, D_1 and D_2 are electronic deformation potentials, which account for the effect of both hydrostatic and uniaxial strain contributions on the A/B energy gap. The D_3 and D_4 are deformation potentials that account for the strain-induced changes of the crystal-field splitting. According to the above equations, the strain induced changes in gap energies can be simplified as follows:

$$E_{A/B}(\varepsilon) = E_{A/B}(0) + (a_{cz} - D_1 - D_3)\varepsilon_{zz} + (a_{ct} - D_2 - D_4)(\varepsilon_{xx} + \varepsilon_{yy}), \qquad (2.6)$$

$$E_C(\varepsilon) = E_{A/B}(0) + \Delta_{cr}(0) + (a_{cz} - D_1)\varepsilon_{zz} + (a_{ct} - D_2)(\varepsilon_{xx} + \varepsilon_{yy}). \qquad (2.7)$$

2.3.2 Piezoelectric fields

In wurtzite-structured group III-nitrides grown on c-plane sapphire substrate, strain induced piezoelectric polarization can be expressed as

$$P^{pz} = e_{31}(\varepsilon_{xx} + \varepsilon_{yy}) + e_{33}\varepsilon_{zz}, \qquad (2.8)$$

where e_{31} and e_{33} are piezoelectric constants, ε_{xx} and ε_{yy} are the in-plane strain, and ε_{zz} is the out-of-plane strain. For biaxial strain, the relation between the in-plane and out-of-plane strain can be expressed as

$$\varepsilon_{zz} = -2\frac{C_{13}}{C_{33}}\varepsilon_{xx}, \qquad (2.9)$$

where C_{13} and C_{13} are elastic constants. Accordingly, the amount of the piezoelectric polarization can be determined as

$$P^{pz} = 2\varepsilon_{xx}(e_{31} - e_{33}\frac{C_{13}}{C_{33}}). \qquad (2.10)$$

Because $(e_{31} - e_{33}\frac{C_{13}}{C_{33}}) < 0$ for $In_xGa_{1-x}N$ over the whole range of compositions, P^{pz} is always negative for layers under biaxial tensile strain and positive under compressive strain. Consequently, the alignment of the spontaneous and piezoelectric polarization will be parallel under tensile strain, and antiparallel under compressive strain as shown in Fig. 2.5.

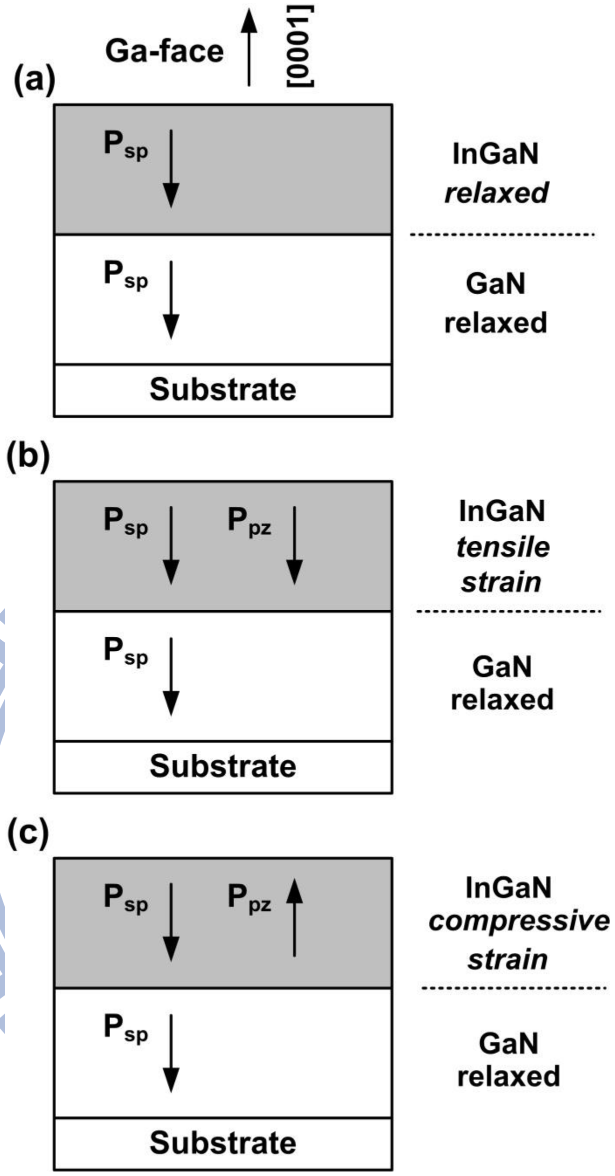

Fig. 2.5: The directions of the P_{SP} and P_{PE} in Ga-polar strained and relaxed InGaN/GaN heterostructures.

For calculating piezoelectric field in $In_xGa_{1-x}N$, the piezoelectric constants (e_{31} and e_{33}) must be known and the values were usually linearly interpolated between InN and GaN. Table 2.4 and 2.5 show some reported values of e_{31} and e_{33} for GaN and InN. For GaN, the constants are more scattered and the values from theoretical prediction is 30 % larger than experimental results. On the contrary, the InN values are less scattered due to the limited data available.

Tab. 2.4: Piezoelectric constants for GaN from the literatures.

GaN	e_{33} (Cm^{-2})	e_{33} (Cm^{-2})	Ref.
Theoretical			
	-0.49	0.73	56
	-0.32	0.63	57
	-0.42	0.57	58
	-0.46	0.78	59
Experimental			
	-0.32	0.58	60
	-0.31	0.56	61

Tab. 2.5: Piezoelectric constants for InN from the literatures.

InN	e_{31} (Cm^{-2})	e_{33} (Cm^{-2})	Ref.
Theoretical			
	-0.57	0.97	56
	-0.59	0.95	58
	-0.48	1.06	59
Experimental			
	-0.55	0.95	61

During 1997-2002, many piezoelectric constants have been calculated by first-principle method [57-59]. Among them, the values for GaN reported by Bernardini *et al.* seem to be much more reliable because they are in agreement with the previous calculation and some experimental results such as laser interferometric technique [60]. However, a significant discrepancy of about 40 % for values of GaN is also observed between the calculated and measured results by the same method [62]. In 2003, Hangleiter *et al.* reported an experimental determination of internal piezoelectric field in InGaN/GaN quantum wells with different In compositions [61]. From the dependence of the electric filed on In composition, they derived the piezoelectric constants e_{31} of GaN and InN. While the values for GaN is about 20 % below the theoretical value. The value for InN is in good agreement with theoretical data. In

2005, Ursula M. E. Christmas *et al.* used an effective-mass model to further investigate the effect of uncertainty in the piezoelectric constants on the internal field and ground state transition in an InGaN/GaN quantum well. They found that the piezoelectric constants provided by Shimada *et al.* [57] can give the best fit to the results in the literature for piezoelectric field and transition energy. Therefore, in the thesis, we will adopt these values to estimate and discuss the piezoelectric fields in InGaN/GaN heterostructures.

Chapter 3 $In_xGa_{1-x}N$ Nanostructures Grown by Metalorganic Chemical Vapor Deposition

3.1 Introduction

In the passed several years, low-dimensional nanostructures such as nanowires and nanodots (islands) have been widely studied due to their inherent superior properties. Among them, $In_xGa_{1-x}N$ nanostructures have attracted a lot of interest because of their potential use in conventional and quantum photonics applications. Therefore, it has become an important subject to further understand the fundamental properties of InGaN nanostructures. However, it remains challenging to synthesize high quality InGaN nanostructures, especially for the In-rich alloys using MOCVD growth.

In the chapter, we shall discuss our recent studies on the structural and optical properties of $In_xGa_{1-x}N$ nanostructures grown by MOCVD. In sec. 3.2, structural and optical characterization of In-rich $In_xGa_{1-x}N$ islands are discussed. Two main subjects are included in this section. First, size dependent strain relaxation in InN islands is presented. Raman measurements on InN/GaN islands of various sizes and shapes grown by different conditions are discussed. The second part of this section is a study of In-rich $In_xGa_{1-x}N$ islands. We investigated the In-rich $In_xGa_{1-x}N$ islands (with $x > 0.87$) grown at various temperatures by MOCVD. Atomic force microscopy (AFM), x-ray diffraction (XRD), photoluminescence (PL) measurements and near-field scanning optical microscopy (NSOM) were employed to study the correlation among surface morphologies, alloy compositions and PL emission bands of these In-rich $In_xGa_{1-x}N$ islands.

In sec. 3.3, we employed the reciprocal space mapping (RSM) to study the strain and composition distribution in Ga-rich $In_xGa_{1-x}N$ films. Optical properties of strained and relaxed phases are discussed. Besides, the correlation between emission efficiency and localization effect in two phases are also presented.

3.2 In-rich $In_xGa_{1-x}N$ island

The growth of InGaN alloys has been predicted to be challenging especially for high In content. The difficulty arises not only from the large lattice match between InN and GaN (~11 %) but also from the high vapor pressure of N_2 over InN. Consequently, phase separated or low crystalline quality $In_xGa_{1-x}N$ films with $x > 0.2$ have been grown by MBE [63] and MOCVD [29,64-65] methods before 2000. After the recent remarkable advances in material growth, single phase $In_xGa_{1-x}N$ alloys ($0.06 < x < 0.97$) have been successfully grown by MBE [66,67].

In addition to the progress in thin film growth, the fabrication of In-rich $In_xGa_{1-x}N$ islands also developed during the last few years [68-73]. Such nanostructures have attracted much attention due to the possibilities in forming a low-dimensional system with large confinement energy. However, the growth of high-quality In-rich $In_xGa_{1-x}N$ island is still not well established.

The major difficulty in In-rich $In_xGa_{1-x}N$ island growth is large lattice mismatch between the epilayer and the substrate material. To our knowledge, strain in the heteroepitaxial growth can be released elastically or plastically, depending on the lattice mismatch and the surface energy. Ng. *et al.* (2002) reported that the InN islands can be fromed on GaN via the Stranski-Krastanov (S-K) mode [74]. It was proposed that InN surface islanding starts as the 80 % of the total strain has been relieved through the formation of defects. In 2006, Lozano *et* *al.* further observed the strain state on InN quantum dots (QDs) on GaN/sapphire substrate by transmission electron microscopy (TEM) [75]. They clearly indicated that the InN QD is almost completely relaxed (97 ± 6 %) by the formation of misfit dislocations (MDs) in the interface area, and a very low percentage of strain is relieved by surface islanding. However, most of the published contributions are focused on the measurement of the residual strain. Only a few reports studied the strain evolution process of In-rich $In_xGa_{1-x}N$ islands [76]. Consequently, it is less clear whether and how the strain release via surface islanding.

In addition to the strain effect, solid phase miscibility gap in In-rich $In_xGa_{1-x}N$ alloys is also a controversial issue. Ho and Stringfellow [77] (1996) firstly pointed out that the solubility of In in GaN is less than 6 % at 800 ^{o}C growth temperature. This prediction is immediately proved by experimental observation from X-ray diffraction (XRD) in InGaN films by Singh *et al.* [28] (1996). In the early 2000s, the phase separation is also evident continuously through systematic investigations such as TEM or Raman measurements [65,78-79]. Although this deleterious effect is hardly being avoided, it has been widely used for forming nanoscale In-rich regions in the last decade. Because such nanostructures were believed to act as “quantum dots” for localizing carriers and were considered to play a key role in the high radiative efficiency of InGaN-based LEDs [10,80]. In this context, self-assembled island growth of InGaN/GaN dots appears to be a more controllable way for realizing such In-rich nanostructures [81-84]. However, the $In_xGa_{1-x}N$ islands reported to date are still in the Ga-rich side ($x < 0.5$), with typical emission wavelength in the blue-green range. On the In-rich side ($0.5 < x < 1$), the $In_xGa_{1-x}N$ islands with NIR emissions are still less studied.

In this section, the initial stage of In-rich $In_xGa_{1-x}N$/GaN heteroepitaxial growth by using MOCVD has been studied. The strain state, structural properties, optical properties and even nucleation process of In-rich $In_xGa_{1-x}N$ islands have been investigated. Firstly, Raman measurements on InN/GaN islands of various sizes and shapes grown by MOCVD using different growth conditions is presented. The Raman frequency is found to shift with the island size, indicating a size dependent strain relaxation during the island formation. We show that the residual strain after plastic relaxation at the InN–GaN interface is further relieved elastically via surface islanding. The second part of this section is a study of In-rich InGaN islands. We investigated the In-rich $In_xGa_{1-x}N$ islands (with $x > 0.87$) grown at various temperatures by MOCVD. Atomic force microscopy (AFM), x-ray diffraction (XRD), photoluminescence (PL) measurements and near-field scanning optical microscopy (NSOM) are employed to study the correlation among surface morphologies, alloy compositions and PL emission bands of these In-rich $In_xGa_{1-x}N$ islands.

3.2.1 Experimental details

InN islands were grown on (0001) sapphire by MOCVD using trimethylgallium (TMGa), trimethylindium (TMIn) and ammonia (NH_3) as precursors. After the growth of a 2-μm GaN buffer layer at 1120/ ℃, the temperature was lowered to 625-700 ℃ for growing InN islands. Different gas-flow sequences and growth temperatures were used to control the InN island size. Two series of samples were prepared. The first series was grown by the so-called flow-rate modulation epitaxy (FME) using alternately injected TMIn [150 SCCM (SCCM denotes centimeter per minute at standard temperature and pressure, STP)] and NH_3 (18000 SCCM) gas flows. A small NH_3 background flow (500 SCCM) was supplied during the TMIn periods [85]. Three FME samples have been grown at 625, 650 and 700 ℃. Another series was grown by the same gas-flow sequence except that a high NH_3 background flow (10000 SCCM) was used. Such a growth method is similar to the so-called pulsed mode (PM), where the NH_3 flow rate was kept high, but the TMIn was pulsed injected. Three PM samples have been grown at 700 ^{o}C using different TMIn injection time $t_{\mathrm{In}} = 10$, 15 and 20 s to control the island size.

The growth method of the uncapped $In_xGa_{1-x}N$ islands samples is also similar with the InN islands. The $In_xGa_{1-x}N$ islands were grown at temperatures between 550-750 ^{o}C. The precursor flow rates were 1, 150 and 18000 SCCM for the TMGa, TMIn and NH_3, respectively. The only difference is that a 1 SCCM TMGa flow was supplied concurrently with the TMIn flow to grow $In_xGa_{1-x}N$ alloys. During the TMGa and TMIn flow periods, the

NH_3 background flow rate was controlled at 10000 SCCM.

Surface morphology was investigated by atomic force microscopy (AFM). Raman measurements were carried out at room temperature in backscattering geometry (*c*-axis) using the 488-nm line of an Ar^+ laser focused through a microscope objective into a spot of ~2 μm. The scattering light was analyzed by a 1-m double monochromator with a spectral resolution 0.9 cm^{-1} and a peak uncertainty of about ± 0.2 cm^{-1}. PL measurements were carried out at $T = 10$ K using the 325-nm line of a He-Cd laser as an excitation source. The PL signals were analyzed by a 0.5 m monochromator and detected by either a photomultiplier tube or a cooled extended InGaAs detector (with a cutoff wavelength at 2.05 μm) for the visible and NIR spectral ranges, respectively. For NSOM measurements, a fiber tip was mounted on a tuning fork of an AFM system for simultaneous measurement of the surface morphology and emission signal using the illumination-collection mode. The tip-sample distance was kept at ~30 nm controlled by the shear-force feedback mechanism.

3.2.2 Size distribution of InN islands

It is well known that the islands size can have a great influence on optical properties such as quantum confinement effect or strain relaxation process. Therefore, how to well control the InN island size becomes important for further understanding this novel material. In general, several methods have been proposed to control InN island size grown by MOCVD such as ammonia background flows or growth temperatures.

Figure 3.1 shows AFM micrographs of InN islands grown at 600 °C by FME and Pulsed mode method with different NH_3 background flow rates (r_0) ranging from 0 to 10000 SCCM [Figs. 3.1(a) – 3.1(e)] and by the conventional growth mode [Fig. 3.1(f)]. The island density and average diameter as function of r_0 are plotted in Fig. 3.1(g). As r_0 was increased from 0 to 10000 SCCM, the island density increased from 6.2×10^{8} to 1.0×10^{10} cm^{-2}, whereas the average base diameter decreased from 350 to 95 nm. Comparing the dot density and size to those obtained by conventional growth mode [indicated by arrows in Fig. 3.1(g)], FME growth under low NH_3 background flows ($r_0 < 1000$ SCCM) generally yields much larger and less dense dots. This can be attributed to the enhanced surface migration of In adatoms in low NH_3 ambience during the deposition of In species [86,87]. As more NH_3 are injected during TMIn periods, surface migration of In adatoms is considerably hindered due to the exposure to a highly N-rich ambience, leading to higher dot densities and smaller dot sizes.

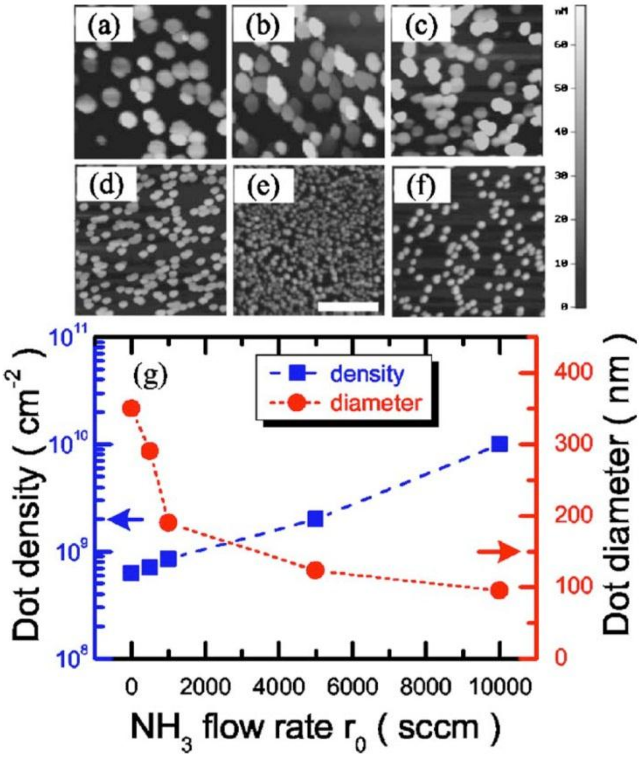

Fig. 3.1: AFM micrographs of InN dots grown by FME and Pulsed mode with different r_0: (a) 0 SCCM, (b) 500 SCCM, (c) 1000 SCCM, (d) 5000 SCCM, and (e) 10000 SCCM, and (f) by the conventional growth mode. (g) The density and diameter of the InN dots as function of r_0.

In addition to ammonia background flow, growth temperature is also an important parameter to determine the island size. Fig. 3.2 shows the statistics of island size distribution at different growth temperatures grown by FME (r_0 = 1000 SCCM) and conventional MOCVD methods.

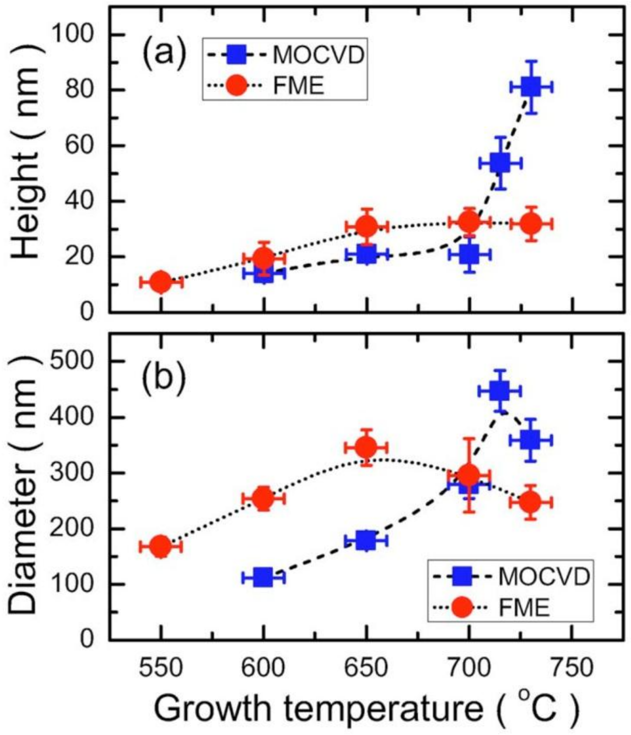

Fig. 3.2: (a) The average island height and (b) diameter of the InN islands grown by the FME and the conventional MOCVD methods as a functions of T_g.

The average height of FME islands increases from 11 to 30 nm as T_g was increased from 550 to 650 ℃ [see Fig. 3.2 (a)]. At still higher T_g, the average height remains constant at ~30 nm. In contrast, the average height of MOCVD islands increases continuously even for $T_g >$ 700 ℃, reaching 80 nm at 730 ℃. Apart from the island height, their base length also changes with the growth temperature, as evidenced in Fig. 3.2 (b). It is worth to note that the aspect ratio (height-to-diameter ratio) of the InN islands generally increase with the increasing T_g. For MOCVD islands, the aspect ratio is typically around ~1/10 for $T_g <$ 700 ℃ and increases to ~1/4 at T_g = 730 ℃. On the other hand, the FME islands are flatter than MOCVD islands, with an aspect ratio of ~1/16 at T_g = 550 ℃ and increases to ~1/8 for $T_g >$ 650 ℃.

According these works, we have obtained that InN islands with controlled size and density can be formed on GaN by using different precursor injection schemes and growth temperatures in MOCVD. These results will help us to further study the size dependent optical properties of InN islands.

Figures 3.3 (a) and (b) show the typical surface morphology of InN islands grown at 700 ^{o}C by using the PM and the FME methods, respectively. The island's shape is hexagonal with a truncated flat top and steep faceted sidewalls. As shown in Fig. 3.3 (a), the PM-grown islands have rather good size uniformity with flat shape and a typical aspect ratio (height/base) less than 0.05, depending on the depositing time. However, for the FME-grown islands, the size distribution is widespread. For the sample shown in Fig. 3.3 (b), the island height (diameter) is from 6 to 60 nm (50 to 500 nm), with an aspect ratio ranging from 0.02-0.26. Such a widespread size distribution allowed us to study InN islands of different sizes and shapes on the same wafer, so that the influence of growth conditions, particularly the growth temperature, on the strain state can be examined.

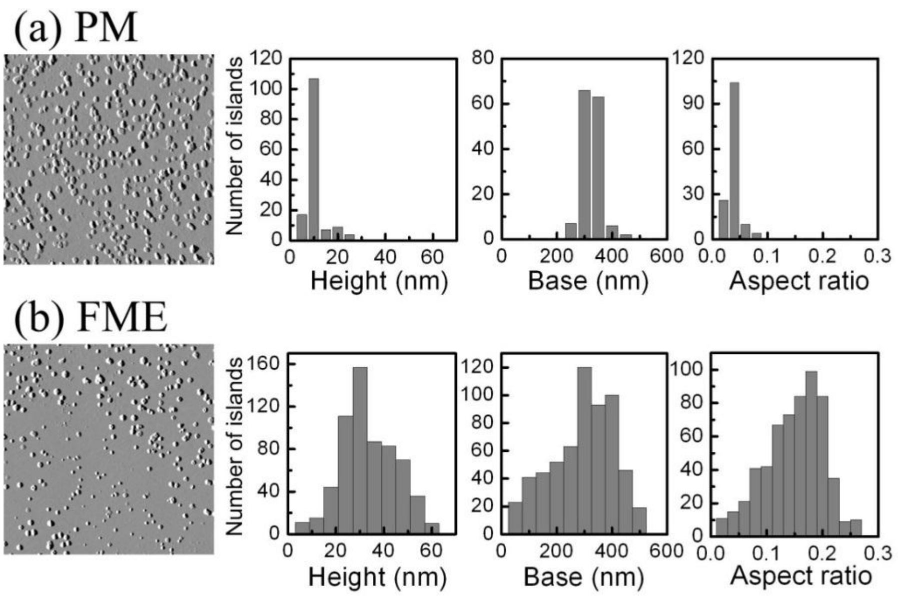

Fig. 3.3: AFM images (10 x10 μm^2) and dots size distribution of InN islands grown by (a) the PM and (b) the FME at 700 ^{o}C.

3.2.3 Size dependent strain relaxation

Before performing the Raman measurements to study the size dependent strain relaxation, we have to realize the size distribution within the laser spot. Typically, the laser illuminating spot covers a total of ~10-20 individual islands. Therefore, we have fabricated an array of markers on the sample surface. This will help us to precisely control the position of laser spot with an accuracy better than 0.5 μm, so that the information about the island size can be obtained from AFM analysis. This laser marking technique is shown schematically in the Fig. 3.4. By inspecting different areas on the wafer, it is possible to locate some particular region, where the island sizes are similar. Accordingly, Raman spectra for InN islands of different

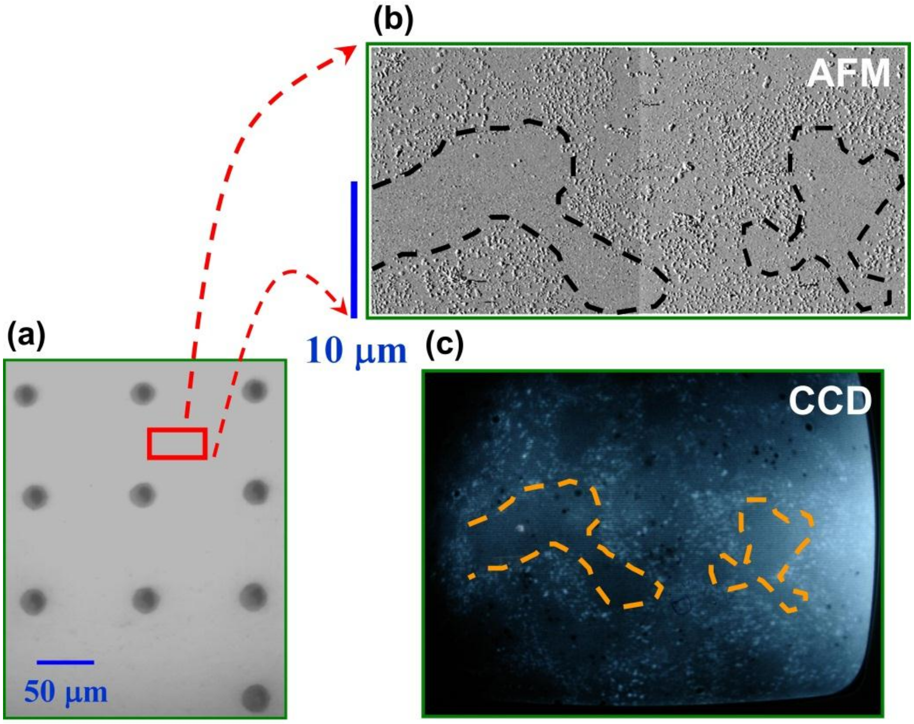

Fig. 3.4: (a) Laser markers fabricated by pulsed laser. (b) AFM image of sample surface and (c) CCD image of sample surface. (b) and (c) are the same areas of sample surface.

sizes were obtained.

In Fig. 3.5, four representative Raman spectra for different island sizes grown either by the PM or the FME are displayed, together with a spectrum obtained from a 300-nm InN thin film. Beside the three peaks from sapphire, the InN E_2-high mode near 490 cm^{-1} can be observed. The Raman frequencies of InN islands are higher than that of the InN film, indicating that islands are more compressively strained than the thin film. In particular, we found that the Raman frequency of the InN islands redshifts with the increasing island size, indicative of a size-dependent strain relaxation in the InN islands.

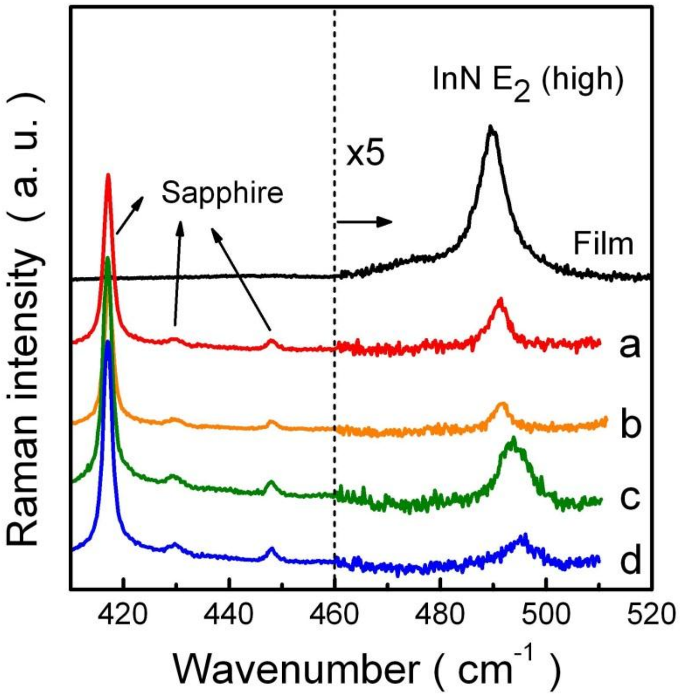

Fig. 3.5: Four representative Raman spectra for InN islands of different sizes grown by the FME [(a) and (b)] and the PM [(c) and (d)] methods. The average island height (base diameter) for (a), (b), (c), and (d) are 47 (202), 38 (180), 22 (310) and 11 (320) nm, respectively. A spectrum taken from a 300-nm InN film is also included.

Figure 3.6 (a) shows the measured E_2-high-mode frequency of InN islands as a function of their aspect ratio (γ). A redshift in the Raman frequency with the increasing γ can be seen, regardless of how the InN islands were grown. In fact, we have also analyzed the Raman frequency as a function of island's height or diameter [75], but the data are more scattered. This leads us to conclude that the decreasing E_2-high-mode frequency with the island aspect ratio appears to be a general trend.

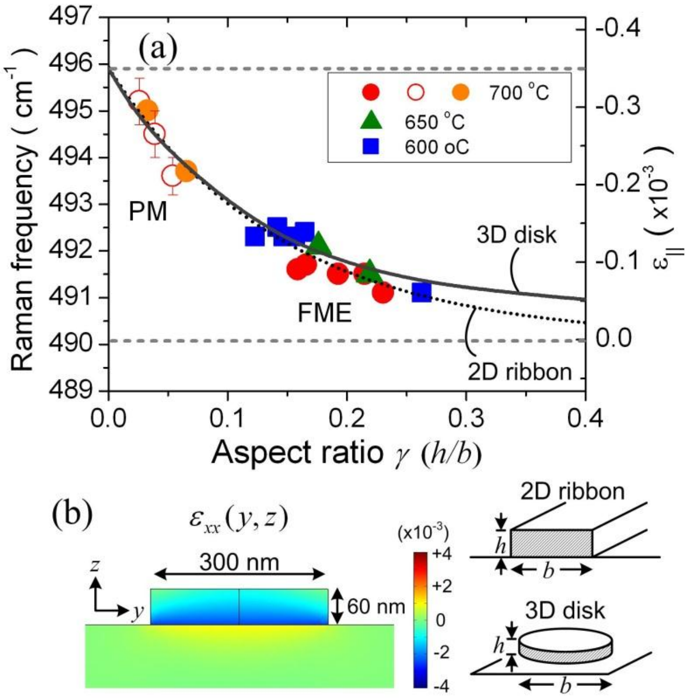

Fig. 3.6: (a) The measured Raman frequency as a function of aspect ratio. The solid (hollow and half-filled) symbols are data obtained from FME (PM) samples grown at different temperatures. The hollow circles with error bars are from PM grown islands with t_{In} = 10, 15, and 20 s. The two half-filled circles are from different regions of the sample with t_{In} = 10 s. The dotted line is the exponential fitting curve. The solid line is the average in-plane strain in disk-shaped islands calculated from 3D finite-element simulations. (b) Simulated distribution of ε_{xx} in the *y*-*z* plane of an uncapped disk-shape island.

The measured Raman shifts can be used to determine the in-plane strain $\varepsilon_{||}$ in the InN islands of different sizes. Here we adopt the values reported in Ref. **63**, where the strain-free Raman frequency and the slope coefficient $\Delta\omega/\Delta\varepsilon_{||}$ of the InN E_2-high mode was determined to be $490.1\,\mathrm{cm}^{-1}$ and $-1660\pm140\,\mathrm{cm}^{-1}$, respectively. As shown by the right scale of Fig. 3.6 (a), the in-plane strain $\varepsilon_{||}$ of these InN islands is compressive (negative), decreasing from -3.1×10^{-3} to -0.6×10^{-3} with the increasing γ from 0.026 to 0.26. It can be inferred that the in-plane strain would approach zero for $\gamma \gg 1$, i.e., the limiting case of a column-like structure. On the other hand, as $\gamma \sim 0$ (i.e., an infinite platelet structure), the measured in-plane strain would represent the initial strain $\varepsilon_{\parallel}^{0}$ at the InN-GaN interface. If we use the exponential function $\varepsilon_{\parallel}(\gamma) = \varepsilon_{\parallel}^{0}\exp(-\lambda\gamma)$ with λ as a fitting parameter to approximate the decreasing in-plane strain, the initial strain can be determined to be $\varepsilon_{\parallel}^{0} = -3.5\times10^{-3}$, with the parameter $\lambda = 6.9$. Since the theoretical lattice misfit for this heterosystem is $f = (a_{GaN} - a_{InN})/a_{InN} = -0.0971$, the deduced $\varepsilon_{\parallel}^{0}$ indicated that at least 96% of the interface strain has been released at the initial stage of island formations. This result is in good agreement with that deduced from the analysis of moiré fringes in high-resolution transmission electron microscopy images by Lozano *et al.* [76,88], where the degree of plastic relaxation was estimated to be 98 % due to the formation of MD network at the InN-GaN interface.

The decreasing in-plane strain with the island's aspect ratio indicates that the residual strain (after the initial plastic relaxation) was further released elastically via surface islanding. In order to know how the residual strain released via the island's free borders, we consider the ribbon model proposed by Kern and Muller [89]. Although this two-dimensional (2D) model is limited to elongated ribbons, it simplifies the problem considerably due to the availability of analytical expression, so that a good approximation for the relaxation of the topmost layers of the InN islands can be obtained [90]. In the model, the in-plane strain in an infinitely long ribbon of height h and base b is given by

$$\varepsilon_{\|}(\gamma, N) = \varepsilon_{\|}^{0} \langle M_1 \rangle^{N-1} \tag{3.1}$$

$$\langle M_1 \rangle = 1 - \frac{2\pi\gamma}{N} + \left(1 + \sqrt{\frac{2\pi\gamma}{N}}\right)^2 \exp(-\sqrt{\frac{2N}{\gamma\pi}}) \tag{3.2}$$

where N is the number of monolayers and $\gamma = h/b$ is the aspect ratio. The equations illustrate that the relaxation depends on both γ and N, while our data [Fig. 3.6 (a)] are a function of γ only. This means that the equations should be further simplified. For the islands sizes investigated here, i.e., $0.02 < \gamma < 0.3$ and $N \geq 28$ ($h \geq 8$ nm), the exponential term in $\langle M_1 \rangle$ is negligible, so that Eq. (3.1) can be reduced to $\varepsilon_{\|}(\gamma, N) = \varepsilon_{\|}^{0}(1 - 2\pi\gamma / N)^{N-1}$. Numerically, as $N > 10$, the expression can be approximated by an exponential function,

$$\varepsilon_{\|}(\gamma) = \varepsilon_{\|}^{0} \exp(-2\pi\gamma) \tag{3.3}$$

which is a function of γ only and independent of N. This explains why the observed in-plane strain decreases exponentially with the aspect ratio. The fitted λ value is also close to 2π, consistent with this simplified model analysis.

The three-dimensional (3D) strain distribution in an uncapped island has also been calculated based on the finite-element method [91]. For simplicity, we consider a disk-shape InN island formed on the GaN surface, with a residual strain of $\varepsilon_{\|}^{0} = -3.5 \times 10^{-3}$ at the InN-GaN interface. The simulated strain distribution of ε_{xx} in the *y-z* plane is shown in Fig. 3-6 (b), where a nonuniform distribution can be seen. By taking the average of the in-plane strain over the entire disk, the calculated results can be compared with the measured Raman data. As shown in Fig. 3-6 (a), the simulated result (solid line) agrees well with the experimental data, further confirming our assertion of size-dependent strain relaxations.

In summary, strain relaxation in uncapped InN/GaN islands of different sizes have been investigated by Raman measurements. A redshift in the Raman peak with the island’s aspect ratio was observed, regardless of how the InN islands were grown. Most of the initial compressive strain at the InN-GaN interface was found to be released plastically, with a relaxation degree up to > 96 %, during the initial stage of island formations. After that, the residual strain of only -3.5×10^{-3}, was further relaxed elastically via the surface islanding. Based on a simplified 2D model analysis and full 3D simulations, we established the relationship of the strain relaxation in InN/GaN islands with their size and shape.

3.2.4 Structural characterization of $In_xGa_{1-x}N$ islands

After the realization of strain relaxation process in InN islands, we further investigate the In-rich $In_xGa_{1-x}N$ islands (with $x > 0.87$) grown at various temperatures by MOCVD. Atomic force microscopy (AFM), x-ray diffraction (XRD), photoluminescence (PL) measurements and near-field scanning optical microscopy (NSOM) are employed to study the correlation among surface morphologies, alloy compositions and PL emission bands of these In-rich $In_xGa_{1-x}N$ dots.

1896

The surface morphologies of $In_xGa_{1-x}N$ dots were studied by AFM. The sample grown at 550 ℃ shows a rough film formed by coalescent islands. For growth temperatures in the range T_g = 600-725 ℃, individual $In_xGa_{1-x}N$ dots were observed, which are shown in Fig. 3.7 (a). With the increasing T_g, the average height and diameter of the InGaN dots increased from 24 to 114 nm and 75 to 410 nm, respectively, whereas the dot density decreased from 4.0×10^9 to 2.2×10^7 cm^{-2}. The dot density as function of T_g is depicted in Fig. 3.7 (b).

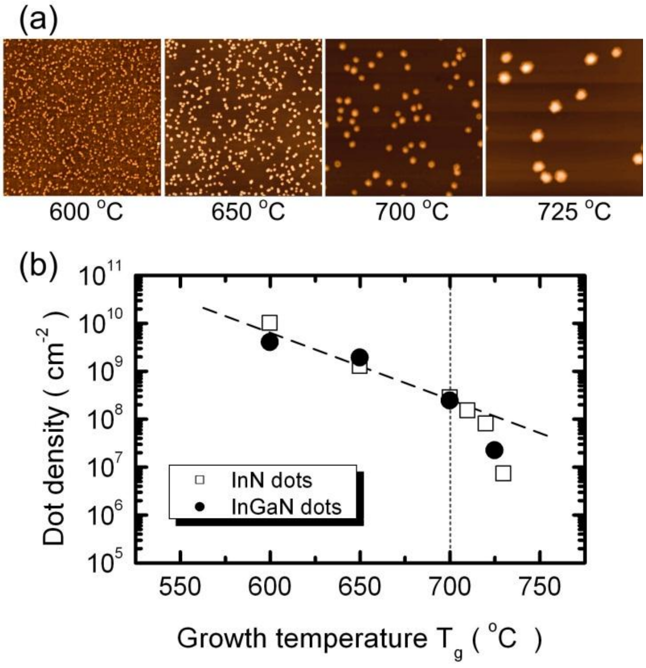

Fig. 3.7: (a) AFM morphology of InGaN dots grown at different temperatures. The images shown are in an area of 5×5 μm^2. (b) The dot density as a function of growth temperature.

In the range of $T_g = 600\text{-}700$ ℃, the decreasing dot density with increasing T_g can be attributed to the enhanced migration length of adatoms, resulting in much larger and less dense dots at higher growth temperatures [85]. For $T_g > 700$ °C, the dot density decreased rapidly and dropped to zero at 750 °C, due possibly to the desorption of metallic In from the growing surface. To further study the nucleation mechanism of InGaN dots, we also prepared a series of samples with InN dots grown at different T_g under similar growth conditions. The density of InN dots as a function of T_g is also included in Fig. 3.7 (b). We found that the densities of InGaN and InN dots show a similar dependence on T_g, implying that the nucleation of InGaN dots is governed by the surface migration of In adatoms, rather than Ga or both. This can be realized from the very different migration capabilities of In and Ga adatoms on the GaN surface. Since the bond strength of InN (7.7 eV/atom) is weaker than GaN (8.9 eV/atom), In adatoms (or its adsorbed precursor molecules) are expected to have a considerably longer migration length on the GaN surface, leading to a much higher nucleation rate and hence governing the formation of InGaN dots.

The In compositions of InGaN dots have been determined by XRD. Figure 3.8 shows XRD $\theta-2\theta$ scans of the investigated samples near the InN(0002) and GaN(0002) diffraction peaks.

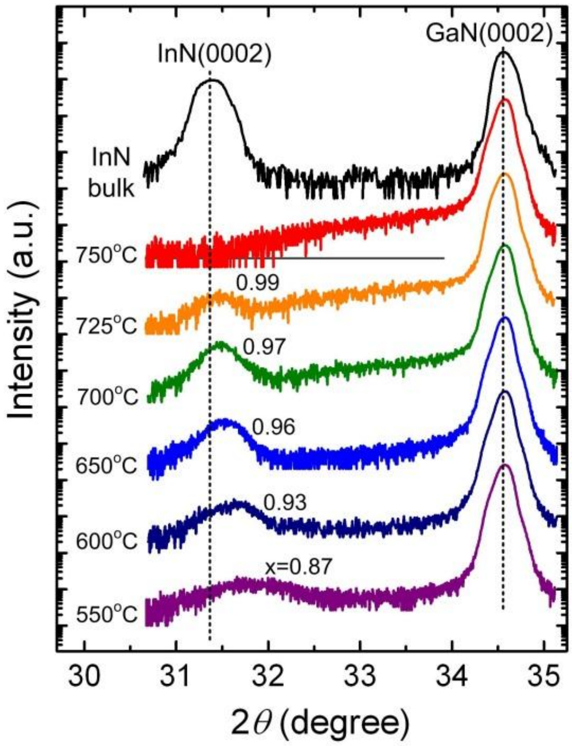

Fig. 3.8: X-ray diffraction of InGaN dots grown at different temperatures.

A diffraction curve of InN film grown on GaN is also included. For the InGaN samples, a broad diffraction peak corresponding to ternary InGaN dots was found to shift gradually toward the InN (0002) peak as T_g was increased from 550 to 725 °C. For the sample grown at 750 °C, the InGaN peak disappeared, due to the complete desorption of In from the growing surface. Using the Vegard's law, we have estimated that the In content (x) of the $In_xGa_{1-x}N$ dots increases from 0.87 to 0.99 as T_g is increased from 550 to 725 °C. This increasing trend is also a consequence of the lower diffusion ability of Ga adatoms. At lower T_g, the growth is under the kinetic-dominant condition, so Ga incorporation at island sites could be dominant. With increasing T_g, the growth conditions become closer to the thermodynamic conditions, which allows the Ga adatoms to select thermodynamically more stable sites and hence hinders the incorporation of Ga adatoms into the In-rich islands. This can be seen from the case of T_g = 725 °C: the $In_xGa_{1-x}N$ dots become highly In-rich, with x up to 0.99. Therefore, it can be inferred that most of the deposited Ga adatoms are distributed among these In-rich islands, forming a thin Ga-rich layer.

To further confirm this assertion, we have also grown a sample with InGaN islands formed on AlGaN/sapphire (0001) at 725 °C. The sample was then investigated by Auger electron spectroscopy (AES) to distinguish the surface composition of In, Ga and Al. Fig. 3.9 (a) and 3.9 (b) are the AES results of surface composition measured on InGaN islands and on flat region without islands, respectively. As shown in Fig. 3.9 (c), after 3 min Ar+ sputtering (with the sputtering rate of 3.5 nm/min) on flat region without islands, the indium signal disappeared, while the Al signal emerged, indicating that a thin Ga-rich InGaN layer was formed among these In-rich islands.

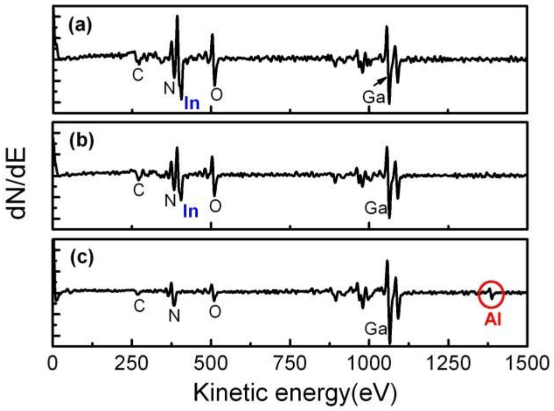

Fig. 3.9: AES of InGaN dots grown on AlGaN buffer layer. Surface composition on dot (a), on flat region among dots (b) and on flat region after 3 min. Ar^+ sputtering (c).

We would like to point out that the deduced In content from Fig. 3.8 does not follow the prediction of equilibrium solubility of GaN in InN based on thermodynamic considerations [77], where the Ga content is expected to increase with the growth temperature. For example, in Ref. 49, the solubility of GaN in InN is predicted to be 3 % at 550 ^{o}C and 6 % at 725 ^{o}C, while our result shows 13 % at 550 ^{o}C and about 1 % at 725 ^{o}C. This clearly indicates that the incorporation of Ga into InN during the growth of InGaN dots is affected by the surface kinetics of In and Ga adatoms rather than equilibrium solubility.

3.2.5 Optical properties of $In_xGa_{1-x}N$ islands

The optical properties of these In-rich InGaN dots were studied by PL measurements. Both the visible and the NIR spectral ranges have been investigated; they are shown in Fig. 3.10 (a) and 3.10 (b), respectively. No PL signal was observed for the 550 ℃ grown sample, since low-temperature growth is detrimental to their optical quality. Samples grown at $T_g =$ 600-725 ℃ exhibit a NIR emission band in the range of 0.77-0.92 eV. A clear redshift in the PL peak energy with increasing T_g can be seen. Since these nanodots are rather large, the energy shift caused by the variation in dot size was estimated to be less than 15 meV, which cannot account for the observed total shift of about 150 meV. Therefore, differences in peak energy between samples must come mainly from the variation of the alloy composition in InGaN dots. In fact, the PL peak energy agrees fairly well with the corresponding In content determined by XRD. Accordingly, we identify the NIR band as the emission from In-rich InGaN dots. For the sample grown at 750 ℃, the NIR band disappeared due to the absence of In-rich islands, which is also consistent with its surface morphology and XRD data. Apart from the NIR band, we also observed a visible emission band in the range of 2.0-2.4 eV for samples grown at $T_g \geq 650$ ℃. Significantly, the visible emission is even stronger for the sample grown at $T_g = 750$ ℃, in spite of the absence of In-rich islands, implying that the visible band does not originated from the InGaN dots.

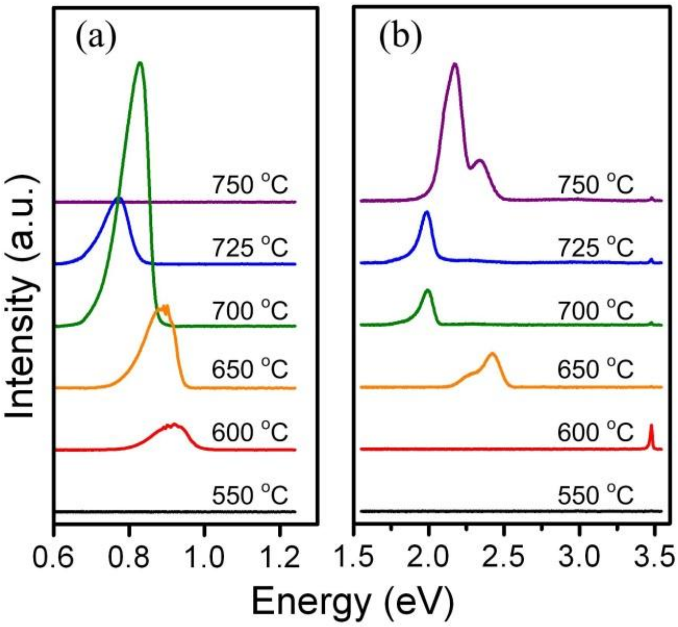

Fig. 3.10: Photoluminescence spectra of InGaN dots grown at different temperatures from 550 to 750 ℃ in (a) the NIR and (b) the visible spectral ranges.

1896

To further clarify this point, we have performed NSOM measurements at room temperature to obtain both the surface morphology and the spatial distribution of visible emissions. Figure 3.11 (a) shows such a NSOM image of the 725 ℃ sample mapping at its visible emission peak. The corresponding surface morphology is shown in Fig. 3.11 (b). It can be clearly seen that these two images are nearly complementary, with dark spots in the NSOM image correspond very well with the In-rich islands revealed in the AFM image. This confirms that the visible emission does indeed originated from the “flat region” outside these In-rich islands. As can be seen from Fig. 3.11 (a), the visible emission is mainly contributed from some bright spots located among these In-rich islands. As mentioned above, the deposited Ga atoms during the growth of InGaN dots may form a thin Ga-rich layer among these In-rich islands, due to the considerable shorter migration length for Ga adatoms. The visible emission band may originate from defect centers induced during the formation of the Ga-rich layer.

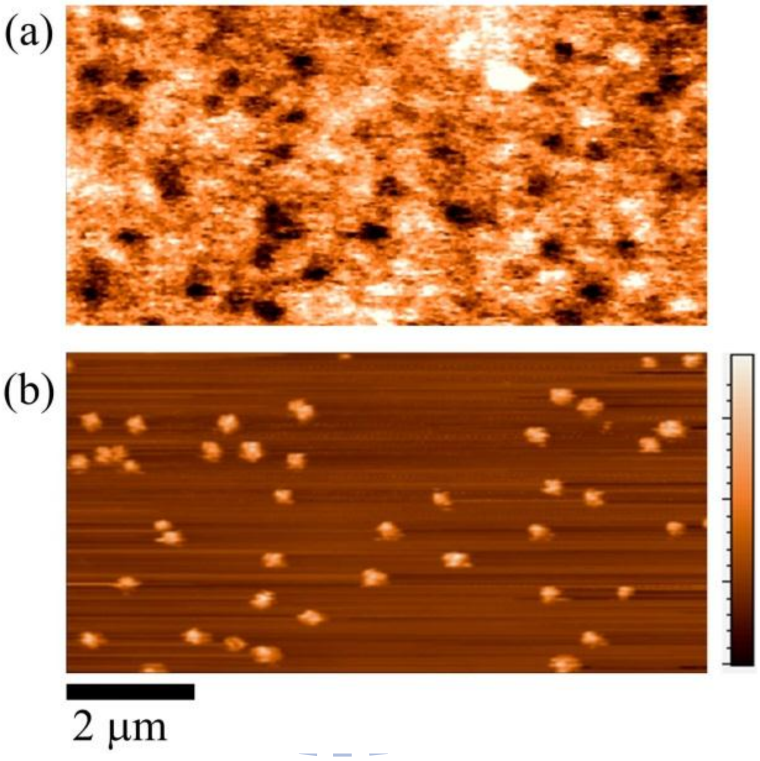

Fig. 3.11: (a) NSOM image of the 725 °C grown sample mapping at its visible emission peak at room temperature. (b) The corresponding AFM image.

In summary, the surface morphologies, alloy compositions and PL properties of In-rich InGaN nanodots grown by MOCVD at $T_g = 550\text{-}750$ °C have been investigated. The nucleation of InGaN dots was found to be dominated by the surface migration of In adatoms. In particular, we found that the incorporation of Ga into InN during the growth of InGaN dots is governed by adatom migration capability, which tends to decompose into In-rich islands and a thin Ga-rich layer at higher growth temperatures. In-rich islands exhibit PL emission in the NIR range, while the formation of a thin Ga-rich layer is likely to be responsible for the observed visible emission band.

3.3 Ga-rich $In_xGa_{1-x}N$ film

Group III-nitride semiconductors have proven their success not only in solid-state lighting, but also in high-power and high-speed electronics [92-94]. Recently, considerable research efforts have turned to the development of III-nitride-based photovoltaic devices [95-97]. In particular, the InGaN alloys with adjustable energy gaps spanning from near infrared (InN) to near ultraviolet (GaN), which covers nearly the entire solar spectrum, are well suited for photovoltaic applications. Indeed, it has been predicted by simulations that the conversion efficiency can be improved to ~30% by using InGaN/Si tandem structures [22].

To realize InGaN-based photovoltaic applications, high-quality InGaN thick layers with relatively high In content as the absorption layers are essential. However, the large lattice mismatch between InN and GaN makes the growth of thick In-rich InGaN layers very challenging [98]. The critical thickness is expected to be less than 100 nm for In contents > 10% [12]. As the InGaN layer exceeds the critical thickness, strain relaxations accompanied by the formation dislocations, composition inhomogeneity [99] or phase separation [28] are frequently observed. Another difficulty arises from the low decomposition temperature for InN (< 700 °C) [100] and the high In desorption rate at growth temperatures > 700 °C. As a consequence, a lower growth temperature is necessary in order to incorporate more In into the InGaN layer. However, lowering the growth temperature is usually accompanied by degraded crystalline quality and hence deteriorated optical properties. Despite these difficulties, InGaN alloys across the entire composition range have been successfully grown by a few groups [33-34,37]. Most of the reported InGaN epitaxial films were grown by molecular beam epitaxy (MBE) [33,37]. Until recently, the growth of thick $In_xGa_{1-x}N$ layers with $x > 0.2$ using metalorganic chemical vapor deposition (MOCVD) has been realized by some groups [40,101]. Growth optimizations [40,102], In composition inhomogeneity and phase separation associated with strain relaxation and p-type doping [101] in thick InGaN layer have also been investigated recently. However, reports on the optical property of MOCVD-grown In-rich InGaN thick layers are still scarce, due mainly to the deteriorated photoluminescence efficiency with increasing In contents.

In the section, the optical properties and carrier dynamics of thick $In_xGa_{1-x}N$ layers with x ranging from 0.13 to 0.38 are investigated by PL and time-resolved PL measurements. The In composition inhomogeneity accompanied by strain relaxations in the InGaN films are studied by high-resolution x-ray diffractions (XRD) and reciprocal space mapping along an asymmetric axis. According to the structural analysis, the observed double PL peaks are associated with the strain relaxation in the InGaN films. Besides, further studies on double peaks are also performed by temperature dependent and time-resolved PL. The optical characterizations such as integrated PL intensities versus temperatures and carrier dynamics are demonstrated clearly. Finally, the correlation between emission efficiency and localization effect is also concluded.

3.3.1 Experimental details

InGaN films were grown on (0001) sapphire by MOCVD using trimethylgallium (TMGa), trimethylindium (TMIn) and ammonia (NH_3) as precursors. After the growth of a 600 nm undoped GaN buffer layer on *c*-plane sapphire substrates at 1130 ^{o}C, the substrate temperature was decreased to 675-750 ℃ for InGaN growth. The precursor flow rates were 1, 100 and 4800 SCCM (SCCM denotes cubic centimeter per minute at STP) for the TMGa, TMIn and NH_3, respectively. XRD and RSM were performed in "PANalytical X'Pert PRO MRD" high resolution diffractometer for symmetric (0002) and asymmetric (105) reflections. PL measurements were carried out at $T = 12$ K using the 325-nm line of a He-Cd laser as an excitation source. The PL signals were analyzed by a 0.5 m monochromator and detected by a photomultiplier tube. For TRPL measurements, we used the 405 nm diode laser as an excitation source and an avalanche photodiode (APD) for detection. The decay traces were recorded using the time correlated single-photon-counting technique with an overall time resolution ~ 180 ps.

3.3.2 Discontinuous strain relaxation in InGaN film

Figure 3.12 (a) shows the XRD $\theta - 2\theta$ scans for the $In_xGa_{1-x}N$ films around (0002) diffraction peaks. The In composition x for each sample was derived from vegard's law. With the decreasing growth temperature (T_g), the In composition was found to increase from x=0.18 to 0.38. The incorporation of more In into the InGaN film at lower growth temperature is mainly due to the lower In desorption rate, particularly when the growths temperature was reduced to below 700 ^{o}C. In Fig. 3.12 (b), the corresponding PL spectra measured at T=12K are displayed. A clear redshift in the PL emission band in accordance with the increasing In composition in the InGaN films can be seen. Besides, for samples grown at $T_g \geq 700$ ^{o}C, the PL emission bands exhibit double peaks. However, only a single XRD peak was resolved in the $\theta - 2\theta$ scans for all the investigated InGaN films. The double PL peak features was usually attributed to the presence of "quantum-dot (QD)-like" or "phase separated" In-rich regions in the InGaN film [103,104]. An alternative interpretation is the occurrence of discontinuous strain relaxations when the thickness of InGaN layer exceeds the critical thickness, resulting in two PL peaks originated from a strained and a nearly fully relaxed regions located at different depths of the film.

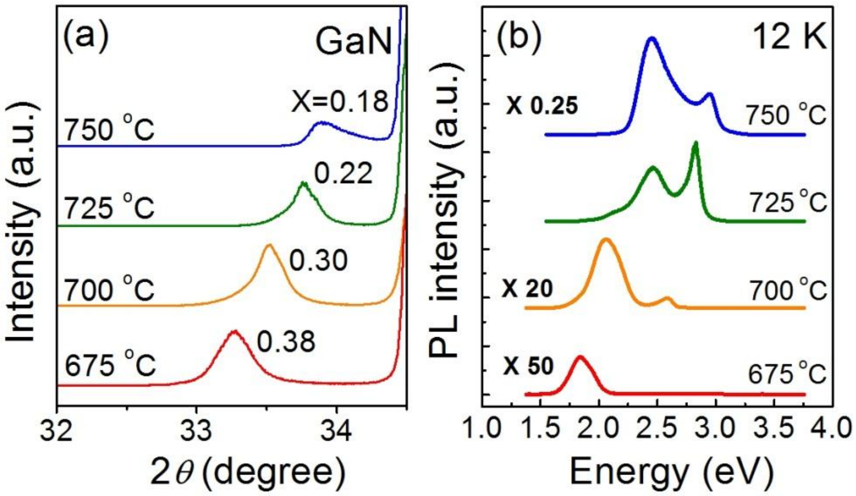

Fig. 3.12: (a) X-ray diffraction and (b) PL spectra of InGaN films grown at temperatures from 675-750 °C.

To clarify the origin of the double peaks, reciprocal space mappings (RSM) of the InGaN films by high-resolution XRD of an asymmetric plane have been performed. By RSM, we measured the out-of plane *c* and in-plane *a* lattice constants, so that from which we extract the In composition *x* including the consideration of the strain state of the InGaN films grown from 675-750 °C, respectively. The scales $Q_x(100)$ and $Q_z(005)$ in unit of rlu are inversely proportional to the lattice constants *a* and *c*, respectively, with rlu denoting $\lambda/2d$, where $\lambda = 0.154056$ nm is the *x*-ray wavelength and *d* is the spacing of parallel planes. According to the measured Q_x and Q_z, the lattice constants *a* and *c* can be determined. The peaks at Q_z= 0.7420 rlu is the GaN diffraction peak, whereas the diffraction peaks below which are originated from the InGaN films. For the 675 °C-grown InGaN film shown in Fig. 3.13 (a), we only observed one InGaN diffraction peak. The corresponding in-plane Q_x is shifted to a lower value (a larger in-plane lattice constant) relative to the GaN peak, indicating that the strain in the InGaN film has been relaxed. As shown in Fig. 3.13 (b)-(d), we found that the diffraction peak for InGaN films grown higher than 700 ^{o}C exhibit a double-peak profile. From measured Q_x and Q_z of the double peak profile, the two peaks are attributed to the coexistence of the two phases in the InGaN films: one is strained [InGaN(*S*)] and the other is relaxed [InGaN(*R*)]. Therefore, we concluded that the observed double PL peaks are associated with the strained and relaxed phases in the InGaN films grown at $T_g \geq 700\,^{o}$C.

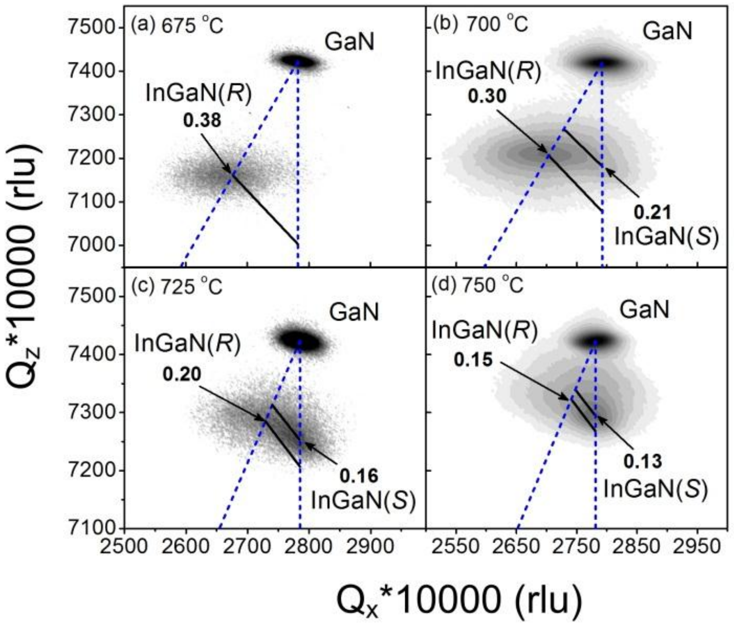

Fig. 3.13: Reciprocal space mapping of InGaN films grown at (a) 675 ^{o}C (b) 700 ^{o}C (c) 725 ^{o}C (d) 750 ^{o}C.

The measured lattice constants a_{InGaN} and c_{InGaN} of the strained and relaxed phases of all the investigated InGaN films are listed in Table 3.1. From these values, we can estimate the In composition *x* and the strain states of different phases according to the Poisson ratio:

$$[\frac{c_{InGaN}-c_0(x)}{c_0(x)}]+2\frac{C_{13}(x)}{C_{33}(x)}[\frac{a_{InGaN}-a_0(x)}{a_0(x)}]=0 \qquad (3.4)$$

where $c_0(x)$ and $a_0(x)$ are the fully relaxed lattice constants extracted from Vegard's law, and $C_{ij}(x)$ are the elastic constants linearly interpolated from the values of GaN and InN. From the parameters of relaxed lattice constants and elastic constants for GaN (a_{GaN}=0.31892 nm, c_{GaN}= 0.51850, C_{13}= 103 Gpa and C_{33}= 405 Gpa) and for InN (a_{InN}=0.35378 nm, c_{InN}= 0.57033, C_{13}= 92 Gpa and C_{33}= 224 Gpa) [53,105-106], we determined the In composition *x* of different phases in all InGaN films, which are also listed in Table 3.1.

Tab. 3.1: The thickness *d*, the lattice constants *a* and *c*, and the In composition *x* of the InGaN films grown at different growth temperatures T_g.

		$In_XGa_{1-X}N$ (*R*)			$In_XGa_{1-X}N$ (*S*)		
T_g (°C)	*d* (nm)	*a* (nm)	*c* (nm)	*x*	*a* (nm)	*c* (nm)	*x*
675	460	0.33225	0.53791	0.38	-	-	-
675	20	-	-	-	0.31971	0.53881	0.25
700	240	0.32906	0.53440	0.30	0.31857	0.53626	0.21
725	330	0.32592	0.52868	0.20	0.31948	0.53093	0.16
750	360	0.32450	0.52593	0.15	0.31994	0.52788	0.13

In all samples, the In composition of the relaxed phase is higher than that of the strained phase. This can also be seen from the RSMs shown in Fig. 3.13, where the asymmetric diffraction profiles are extended continuously between two isocomposition lines, indicative of a composition gradient in the film. Such a variation of In composition can be attributed to the compositional pulling effect, which has been reported in Ref. [107]. The strain exhibit in the InGaN epilayer was considered as the main driven force, which tends to expel In atoms from the epilayer during the initial stage of InGaN growth. As the growth proceeds, the strain in the InGaN layer relaxes gradually, leading to the incorporation of more In atoms into the subsequent InGaN layer. From table 3.1, we also found that the difference in the In compositions of the two phases also increases with the In composition. This further confirms that the strain is the main cause of the compositional pulling effect.

According to the structural analysis, we concluded that the observed double PL peaks are associated with the strain relaxation in the InGaN films. The higher (lower) energy PL peak can be attributed to the emission from the strained (relaxed) phase in the InGaN film. For the sample grown at T_g= 675 ^{o}C, only the relaxed phase and one PL peak were observed. To verify the PL peak assignments, we have also grown an InGaN film at 675 ^{o}C with a nominal thickness d < 20 nm. From the RSM of the thin InGaN film shown in Fig. 3.14 (a), only the strained phase with x = 0.25 is observed. As shown in Fig. 3.14 (b), the PL peak of the strained InGaN film blueshifts to 2.52 eV, significantly higher than the relaxed film at 1.82 eV.

1896

This further confirms that double PL peaks are originated from the strained and relaxed phases in the InGaN films.

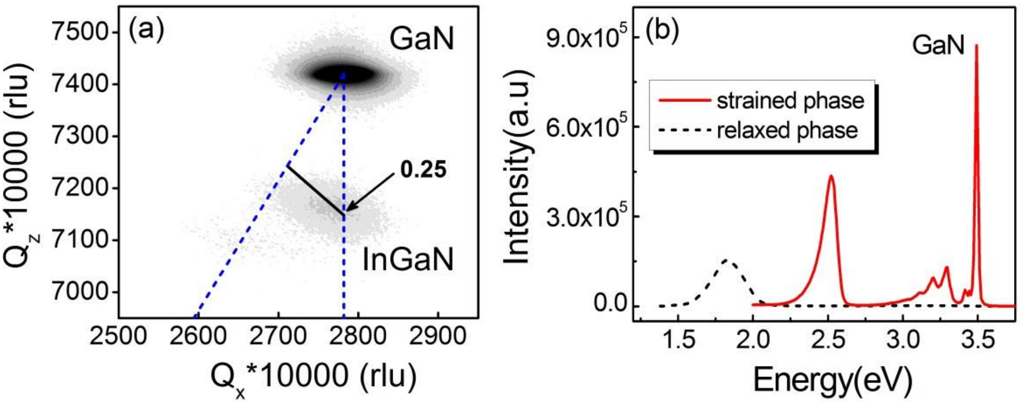

Fig. 3.14: (a) RSM of 20 nm InGaN films grown at 675 °C.
(b) PL spectra of InGaN films with different thickness at 675 °C.

3.3.3 Emission properties of strained and relaxed phase

The optical properties of the double PL peaks associated with the strain relaxation in the InGaN films have been investigated by temperature-dependent PL measurements. Figure 3.15 (a) shows the temperature evolution of PL spectrum for the InGaN film grown at 725 °C. The corresponding integrated PL intensities as a function of temperature for both phases are displayed in Fig. 3.15 (b). The PL intensity of the strained phase decreases more rapidly with increasing temperature when T > 80 K. At room temperature (RT), the PL spectrum is dominated by the emission from the relaxed phase. Figure 3.15 (c) shows the ratio of the integrated PL intensity at RT to that at $T = 12\,\mathrm{K}$, $\eta = I_{PL}(300\,\mathrm{K}) / I_{PL}(12\,\mathrm{K})$ for all samples.

It is evident that the emission efficiency for the relaxed phase is better than the strained phase, regardless of different growth temperatures. However, we noted that the PL efficiency of the InGaN films degraded with decreasing T_g. This is evident from the RT PL intensity for all the investigated samples shown in Fig. 3.15 (d), where the PL intensity decreases by over 3 orders of magnitude as T_g was decreased from 750 to 675 ^{o}C. It is well known that growth temperature plays a decisive role in the growth of In-rich InGaN. Although a lower T_g can incorporate more In content into the InGaN film, it is usually accompanies by more structural defects and hence degraded optical properties.

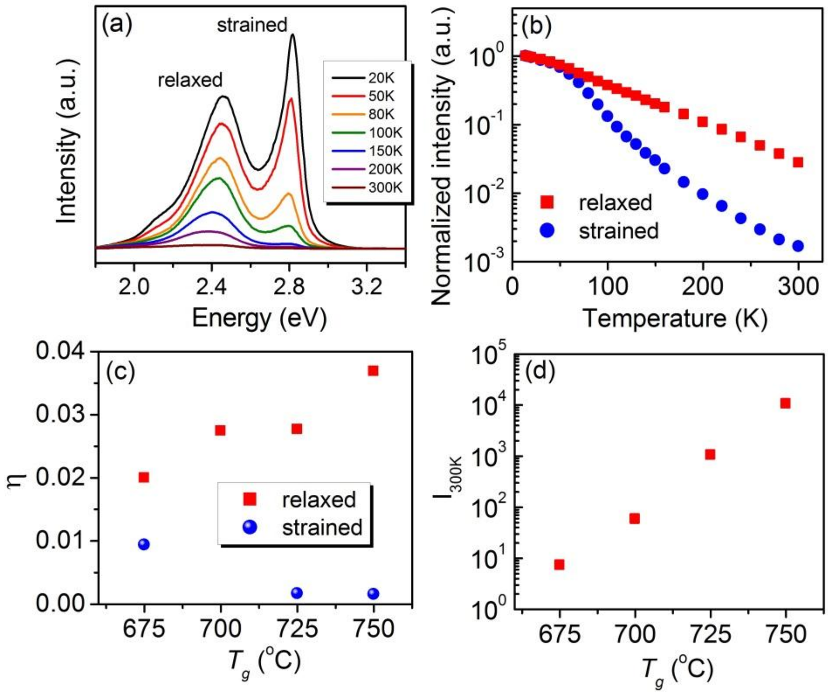

Fig. 3.15: (a) Temperature dependent PL of InGaN film grown at 725 ^{o}C. (b) PL intensity of strained and relaxed phase versus temperature. (c) Emission efficiency of strained and relaxed phase and (d) room-temperature PL intensity of relaxed phase versus growth temperatures.

It is worth to point out that the relaxed phases have superior PL efficiency than the strained phases at RT seem to be counterintuitive, since the relaxed phases are expected to be more dislocated. To clarify this unusual character, we have performed time resolved-PL measurements. Figure 3.16 (a) shows the PL decay traces measured at 12 K for the strained and relaxed phases in the InGaN film grown at 750 ^{o}C. The decay traces for both phases show a non-single exponential decay, which was commonly observed in the In-containing alloys due to the carrier localization effect. The slower PL decay for the relaxed phase can be attributed to a more pronounced localization effect in the relaxed phase due to alloy disorders. In Fig. 3.16 (b), the effective PL decay lifetimes (τ_{eff} at which the PL intensity decreased to 1/e) of the strained and relaxed phase for all samples are displayed. The measured τ_{eff} for the relaxed phase decreases with decreasing T_g, while the measured τ_{eff} for the strained phase is nearly unchanged at about 1 ns for all samples. For the relaxed phase, the decreasing τ_{eff} with the decreasing T_g may arise from the higher defect density formed in the relaxed layer grown at lower temperatures.

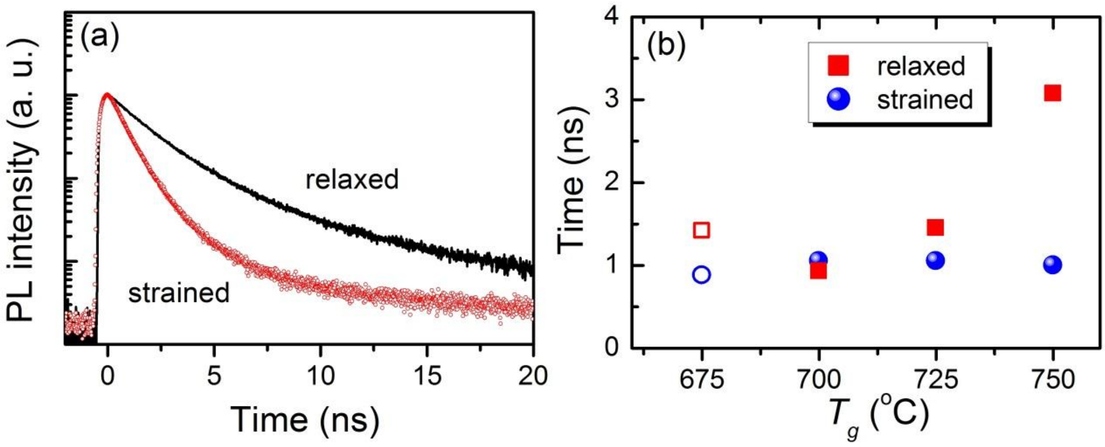

Fig. 3.16: (a) TRPL spectra of strained and relaxed phase at 12 K and (b) the effective carrier lifetimes deduced from decay traces of strained and relaxed phase versus growth temperature.

3.3.4 Localization effects in strained and relaxed phase

The effect of carrier localization can be further investigated by energy-dependent TRPL measurements. In Figs. 3.17 (a) and (b), the time-evolution PL spectra for the strained and relaxed phases in the InGaN film grown at 675^{o}C are displayed. A clear temporal PL redshift is observed for the relaxed film. Such a temporal redshift have been observed in InGaN alloys due to the carrier transfers from localization centers with higher energies to those with lower energies [108]. On the contrary, the temporary PL redshift is absent in the strained film. Similar behaviors have also been observed in samples grown at higher temperatures. Therefore, we conclude that the carrier localization effect is more pronounced in the relaxed phase. This trend can also be explained by the compositional puling effect caused by strain relaxations, leading to inhomogeneous In distribution and the formation of local In-rich regions in the relaxed phase.

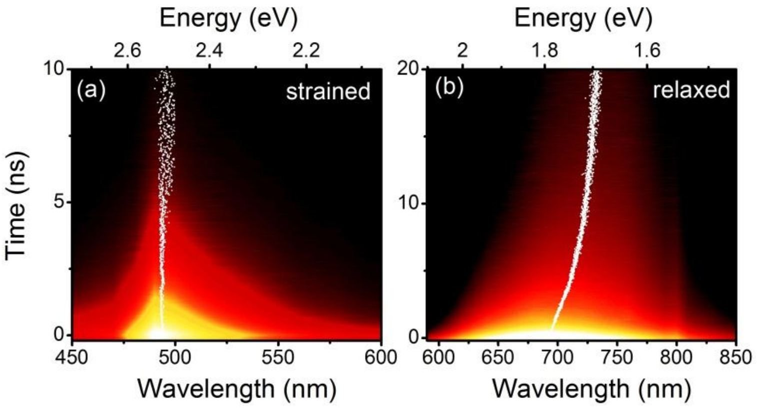

Fig. 3.17: Energy dependent TRPL of InGaN films grown at 675 °C (a) strained phase (b) relaxed phase.

Carriers confined in localization centers, which prevent the carrier diffusions to nonradiative recombination centers, could be the main cause of the superior PL efficiency associated with the relaxed phases at RT. This assertion can be verified by temperature-dependent TRPL measurements. Figure 3.18 shows the measured decay time τ as a function of temperature for the strained and relaxed phases in the InGaN film grown at 725 ^{o}C. The measured $\tau(T)$ can be decomposed into the radiative lifetime τ_r and the nonradiative lifetime τ_{nr} according to $1/\tau = 1/\tau_r + 1/\tau_{nr}$. A standard way to extract τ_r and τ_{nr} from the measured $\tau(T)$ is to determine the radiative efficiency $\eta(T) = \tau_{nr}/(\tau_{nr}+\tau_r)$ according to the measured temperature-dependent PL intensity $\eta(T) = I_{PL}(T)/I_{PL}(12\,\mathrm{K})$, by which the radiative lifetime can be determined using $\tau_r(T) = \tau(T)/\eta(T)$. The deduced $\tau_r(T)$

ES A 1896

and $\tau_{nr}(T)$ are also shown in Fig. 3.18. For the strained phase, the deduced τ_r is nearly constant at temperatures below 50 K, but above which it exhibits a $T^{3/2}$ dependence. The radiative lifetime for a direct band-gap material is related to the effective densities of states in the conduction or valence bands [109], which can be simplified to a temperature dependence of $T^{d/2}$, where d is the system dimensionality. For $T > 50\,\mathrm{K}$ with $d \approx 3$ can be attributed to the recombination processes in bulk materials, while for $T < 50\,\mathrm{K}$ with $d \approx 0$ could arise from the 0-D like transition due to the localizations of carriers in In-rich regions. For the relaxed phase, the effect of carrier localization is more pronounced, which is evident from the higher turning temperature at around 105 K. This verifies that carrier localizations are more pronounced in relaxed phases, leading to the superior emission properties at RT than the strained phase in InGaN films.

1896

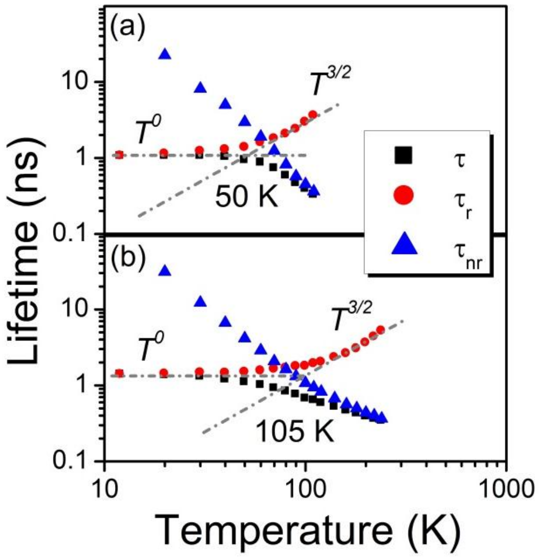

Fig. 3.18: The measured decay time τ as a function of temperature T for (a) strained phase and (b) relaxed phase of InGaN film grown at 725 ^{o}C. The deduced radiaive $\tau_r(T)$ and $\tau_{nr}(T)$ lifetimes are also shown.

In summary, the double PL peaks associated with strained and relaxed phase in the InGaN films were investigated. Formation mechanism of two phases with different strain states is also discussed through the reciprocal space mapping (RSM). By comparing the RSM and PL results, the correlation between emission energies and two phases were demonstrated. According to the temperature-dependent and time-resolved PL (TRPL), it is indicated that the room temperature PL intensity was dominated by relaxed phase and it has been suggested to highly correlate with the defect densities in InGaN films. Besides, we also demonstrate that the more localization centers existed in relaxed phase than strained one from TRPL measurements. Therefore, we can observe the enhancement of the room-temperature PL intensity of relaxed phase even though the existence of more defect densities.

Chapter 4 InGaN/GaN Nanowires Grown by Molecular Beam Epitaxy

4.1 Introduction

Semiconductor nanowire heterostructures are one-dimensional structures which are typically 20-100 nm in diameter and 1-10 μm in length. This axial heterostructures can be used for designing novel nanostructures for exploring new physics or new technologies. Recently, many works have been done in demonstrating the use of single nanowire heterostructures for single photon emitters [110,111], photodectors [112], and single electron devices [113].

In the passed several years, nearly defect-free InGaN/GaN nanowires heterostructures have been successfully grown on Si substrate by MBE. These structures are quite different from commonly used planar heterostructures, which are usually grown on sapphire substrate and have defect densities as high as 10^9-10^{10} cm^{-2}. Therefore, it is advantageous to further discuss the intrinsic material properties, to understand limitations in device performance and for the realization of novel devices. However, many physical properties of InGaN/GaN nanowires are still unclear and have to be clarified.

In this chapter, some structural and optical properties of InGaN/GaN nanowires grown by MBE are discussed. In sec. 4.2, the suppressed piezoelectric field in InGaN/GaN nanowires is evident from the optical spectroscopic investigations. Based on the finite element simulations, the inefficient strain relaxation through the lateral free surface is presented. By combining the composition analysis from STEM-EDX, the possible origin of strain relaxation in InGaN/GaN nanowries is also discussed.

In sec 4.3, band-gap tuning of InGaN/GaN nanowire heterostructures by applying an external stress using a piezoelectric actuator is demonstrated. μ-Photoluminescence (μ-PL) measurement and numerical simulations were employed to study the strain field distribution in 1-D heterostructures. Finally, the correlation between strain field and bandgap variation is also presented.

4.2 Suppressed piezoelectric field in single InGaN/GaN heterostructure nanowires

III-nitride semiconductors have already been an important material for various electronic and optoelectronic devices [114,115]. Of particular importance is the InGaN ternary alloy due to its adjustable band gap from near ultraviolet to near infrared. However, the internal quantum efficiency is limited by the presence of strong polarization fields in InGaN/GaN heterostructures, which tend to separate the electron and hole wave functions and redshift the emission energy due to the quantum confine stark effect (QCSE) [122-125].

Recently, one-dimensional InGaN/GaN heterostructures formed by GaN nanocolumn or nanowires (NWs) with inserted InGaN disk layers [116-121], have been proposed to tackle this problem. Indeed, the absence of excitation-induced blueshift has been observed in either ensemble or single GaN nanorods with InGaN disks insertions [119,122,123]. The insignificant piezoelectric field was attributed to the efficient strain relaxation via the NW sidewalls. On the other hand, recombination lifetime reductions accompanied by small excitation-induced blueshifts (~1-10 meV) have been observed and considered as evidences for the presence of a weak piezoelectric field in InGaN/GaN nanocolumns [124,125]. Recent calculations based on the finite element method (FEM) indicated that the NW geometry can only accommodates marginal elastic relaxations and strong piezoelectric polarizations still reside in the InGaN disk [125-127]. More recently, a green emission band that exhibits strong excitation induced blueshifts and a number of sharp emission lines with peak energies insensitive to excitation density were found to coexist in spectra of single InGaN/GaN NWs. It was argued that strong carrier localizations may be the origin for the absence of QCSE for those sharp emission lines [127].

In this section, we present microphotoluminescence (μPL) measurements on single InGaN/GaN NWs with diameters in the range of 9-27 nm. Sharp emission lines originated from the recombination of localized excitons in the InGaN layers can be resolved at low temperatures. Excitation dependent energy shifts, spectral diffusions, time-resolved PL measurements of these emission lines indicate that the polarization field is insignificant in the InGaN/GaN heterostructures. Composition analyses together with FEM simulations suggest that In-Ga intermixing also play a role in the strain relaxations in InGaN/GaN NW heterostructures.

4.2.1 Experimental details

The InGaN/GaN NW heterostructures were grown on a Si (111) substrate by radio frequency plasma assisted molecular beam epitaxy. Prior to the crystal growth, Si substrate was first cleaned by acetone, methanol, and HF acid for the oxide removal. The substrate was then degassed at 900 ^{o}C in the growth chamber until the formation of a 7×7 surface reconstruction, indicative of a pure Si (111) surface. After the growth of a thin AlN buffer layer on the Si surface, GaN NWs were then grown at 750 ℃ under N-rich conditions (3.5 sccm). A 2-nm-thick InGaN layer followed by a 5-nm-thick GaN capping layer was then grown on top of these NWs. The growth details of the InGaN/GaN NW heterostructure can be found in [128]. Structural analysis indicated that the wire diameter is in the range of 9 to 27 nm, with an average diameter of 18 nm. The wire lengths can be distributed from 1 to 4 μm, depending on the growth time.

Emission spectra of single InGaN/GaN NWs were measured by a low-temperature μPL setup. The measurements were carried out at $T = 6$ K using the 325-nm line of a He-Cd laser as an excitation source. The laser was focused to a spot of about 1 μm in diameter by an objective lens (N.A.= 0.5). The μPL signals were analyzed by a 0.75 m monochromator with a 1200 g/mm grating and detected by a liquid nitrogen-cooled charge-coupled device (CCD), corresponding to a spectral resolution of 0.05 nm (~400 μeV). For time-resolved PL measurements, the excitation source was replaced by either a mode-locked frequency-doubled

Ti-sapphire laser (355 nm/80 MHz) with a 200-fs pulse width or a pulsed diode laser (405 nm/ 40MHz) with a 50-ps pulse width. The decay traces were detected by a fast avalanche photodiode and recorded using the time correlated single-photon-counting technique with a temporal resolution of ~150 ps.

To assess the PL spectrum of single NWs, the deposited NWs were mechanically scratched from the substrate and then dispersed in methanol. The solution was then dropped onto another Si substrate with gold pattern on top. After drying, single NWs were separately dispersed on the substrate.

4.2.2 Structural characterizations

Schematic structure and morphology are depicted in Fig. 4.1 (a) and (b). Isolated NWs were grown in the c-axis (0001) direction and well-aligned, which is a very important advantage since optical collection efficient will be much enhanced from the top. Detailed morphology of single nanowire/column is shown in the TEM image as Fig. 4.1 (c). The morphology could be identified as two regions clearly: the upper very thin wire part, and the simultaneously grown underlying columnar layer with hexagonal crystalline facet. The nanowire density is as low as 6.7x10^8 cm^{-2}, which is 2 order of magnitude lower than SK quantum dots and QD in-a-wire reported.

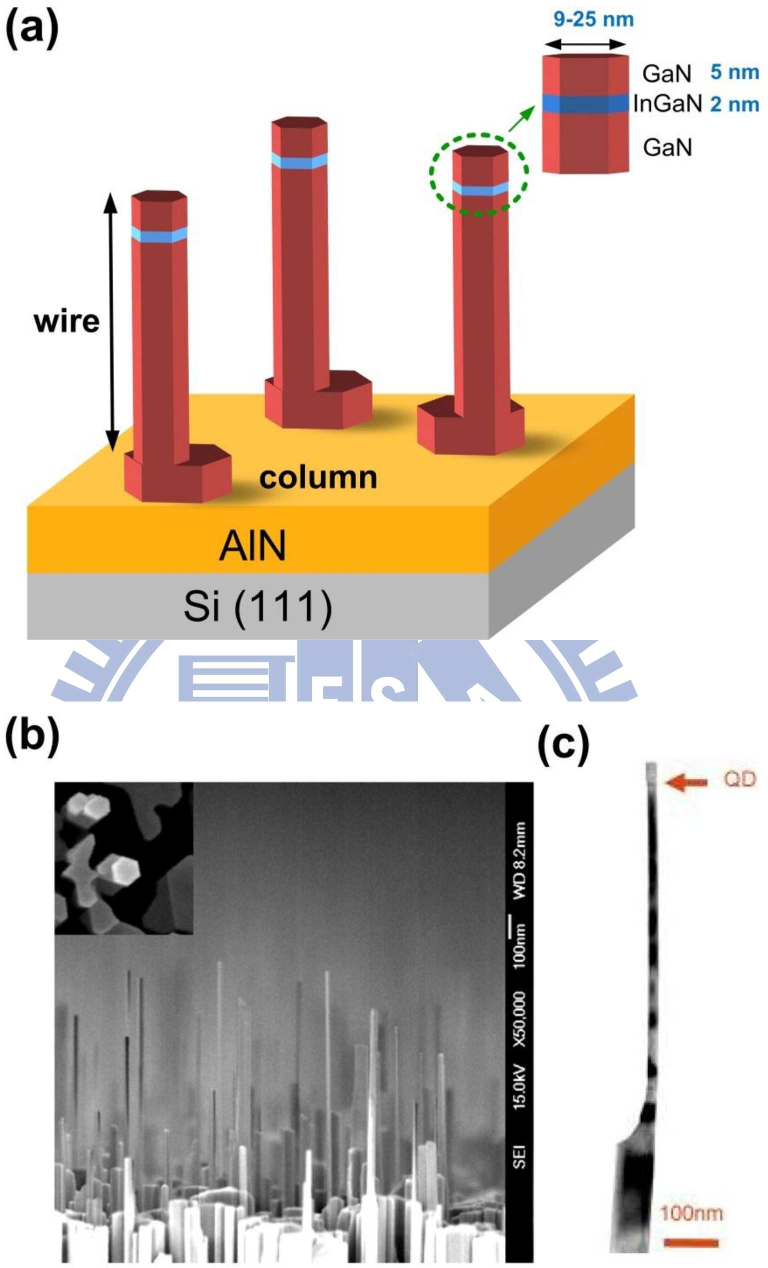

Fig. 4.1: Schematic illustration of InGaN/GaN NWs. The GaN NWs were grown on top of Si(111) and AlN buffer layer. The structure could be divided into nanowires (9-27 nm in diameter) and underlying columns (over 80 nm in diameter), which are grown simultaneously. At the end of the growth, 2 nm InGaN nanodisk was grown and 5 nm GaN was capped on top of it.

4.2.3 Luminescence properties

Figure 4.2(a) shows the typical μPL spectrum of a representative single NW measured at T= 6 K under a cw excitation power of $P_{\mathrm{ex}} = 40\ \mu\mathrm{W}$. Spectral features ranging from 3.3-3.5 eV are attributed to the near-band-edge emissions from the GaN NW. A number of sharp emission lines can be observed at energy below 3.2 eV. This spectral range corresponds to the low-energy side of the InGaN emission band observed in NW ensemble. The line widths of these sharp lines are ranging from 500 μW to ~1 meV. According to previous studies on conventional InGaN/GaN quantum wells (QWs) [129] and quantum dots formed by SK growth [130], these sharp lines can be attributed to the emissions from localized excitons in the InGaN layer. Since the diameter of the investigated NWs is still large in comparison with the exciton Bohr radius in InGaN, the InGaN disk still acts somewhat like a QW without lateral quantum confinements. We have measured many individual NWs and found that the emission energies and the number of sharp lines vary from NW to NW. This indicates that the exciton localizations are likely to arise from some randomly distributed localization centers in the InGaN disk layer caused by thickness and/or alloy fluctuations.

Figure 4.2(b) shows a series of PL spectra for the two emission lines near 2.93 eV (labeled as X and X*) taken under different excitation powers. The integrated PL intensity I_{PL} as a function of excitation power P_{ex} are displayed in Fig. 4.2(c). The power dependence of each line can be characterized by $I_{\mathrm{PL}} \propto P_{\mathrm{ex}}^{m}$, in which the exponent m is a fitting parameter. With increasing P_{ex}, the X line intensity increases almost linearly ($m \approx 0.9$), whereas the X* line exhibits a superlinear power dependence with ($m \approx 1.4$). The X line can thus be attributed to the recombination of single excitons, while the X* line is likely to arise from charged excitons. We also note that there is no apparent intensity saturation for both X and X* lines, which is probably limited by the maximum attainable laser power of our measurement systems.

In Fig 4.2(d), the emission energies of X and X* lines are plotted as a function of P_{ex}. Only a very small blueshift of ~0.46 meV is observed for the X line when the excitation power is increased to 30 μW. In conventional InGaN/GaN QWs, the presence of a strong polarization field (~MV/cm) can lead to an excitation-induced blueshift up a few tens or even hundreds meV's due to the screening of QCSE by the photogenerated carriers. The observed small excitation-induced blueshift is therefore a signature of suppressed polarization field in the investigated InGaN/GaN heterostructure NWs.

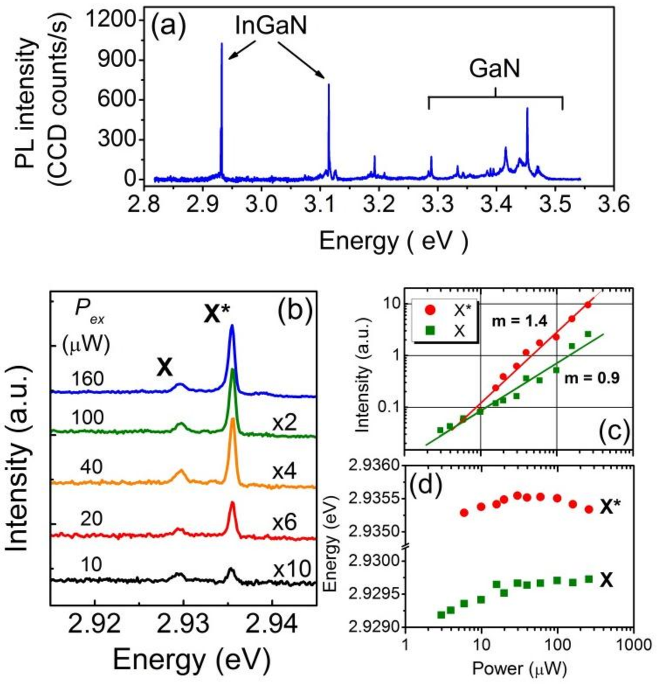

Fig. 4.2 : (a) A typical μPL spectrum taken from a representative single NW. (b) Power-dependent spectra for the emission lines near 2.93 eV (c) Integrated intensities and (d) peak energies of X and X* as a function of excitation power.

We have measured several NWs and analyzed the excitation-dependent spectra of emission lines from the InGaN disk layer. It was found that blueshift with the excitation power is not a general trend for the investigated InGaN/GaN NWs. As shown in Fig. 4.3, blueshifted, redshifted or even constant peak energy with increasing excitation power can be observed in different NWs. This dependence is not anticipated from the screening of QCSE caused by the polarization field in the InGaN/GaN NWs. In addition, the energy shifts are quite small, typically smaller than the line width (< 1meV) of each emission line. Therefore, we suggested that the excitation-induced energy shift is related to the electric field produced by some charged traps in the vicinity of the localization centers. Under optical excitations, the photogenerated carriers can either ionize or neutralize these traps and thereby the average electric field could either be increased or decreased by the increasing excitation power, depending on the initial charge states of these nearby traps.

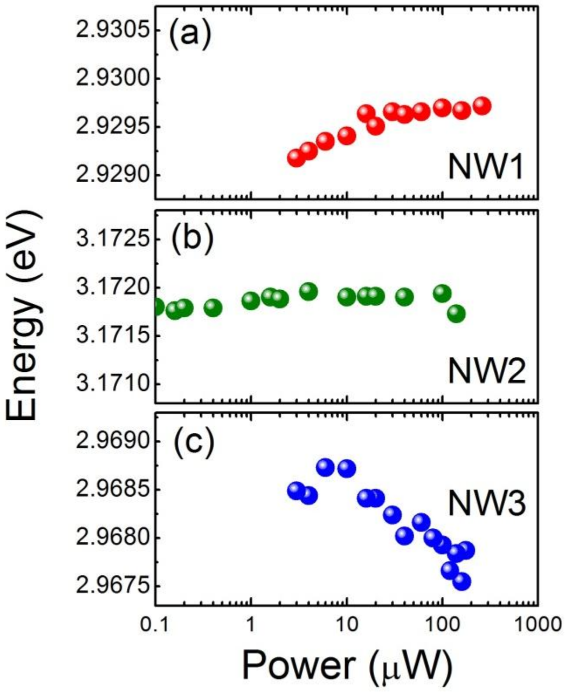

Fig. 4.3 : Peak energy as a function of excitation power for three different InGaN/GaN NWs

The influence of the nearby charged traps can be studied by monitoring the spectral diffusions of these emission lines. Figure 4.4(a) shows the spectra of NW1 near the X and X* lines recorded as a function of time with an integration time of 1 s for each. Although the influences of nearby traps that occur on a time scale shorter than 1 s are averaged, both the X and X* lines reveal spectral diffusions with amplitudes ≤ 0.5 meV. A statistics of the nearly

800 consecutive spectra indicated that the integrated PL intensity and peak energy of X line are correlated. As shown in Fig. 4.4(b), a blueshifted (redshifted) PL peak is accompanied by an enhanced (suppressed) PL intensity. This correlation clearly indicates that the spectral diffusion is caused by the QCSE arising from charge fluctuations nearby. In addition, we also found that the X and X* lines exhibit the same spectral diffusion pattern. This is evident from the data shown in Fig. 4.4(c), where a linear correlation between the peak energies of X* and X is observed, indicating that both lines are originated from the same localization center. It is noteworthy that the spectral diffusion amplitudes of X and X* lines are of the same order as the excitation-induced energy shifts shown in Fig. 4.2(d). The X* line, which is less blueshifted by the excitation power, exhibits a smaller spectral diffusion amplitude. This leads us to conclude that the excitation-dependent energy shifts and the spectral diffusion are all caused by the electric field produced by the nearby charged traps, rather than the polarization field in the InGaN/GaN heterostructures.

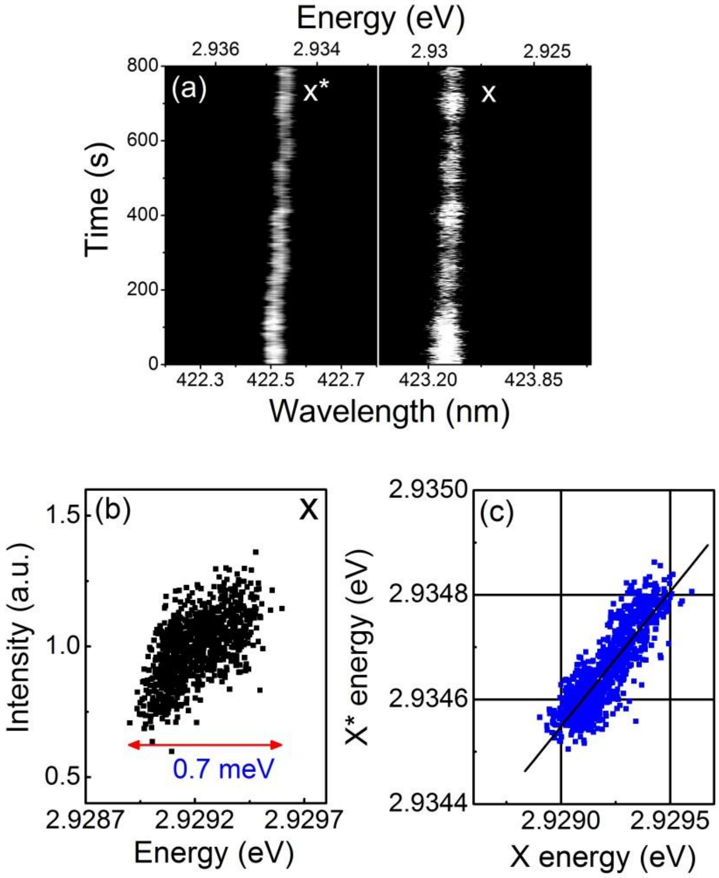

Fig. 4.4 : (a) A contour plot of the time evolution of X and X* lines constructed by consecutive spectra with an integration of 1 s for each. (b) The correlation between the integrated intensity and the peak energy of X line. (c) The correlation between the peak energies of X and X* lines.

Time-resolved PL measurements on individual NWs have also been performed and the data are shown in Fig. 4.5(a). The decay traces can be fitted by a single exponential function with a decay lifetime ranging from 200-620 ps. The short lifetimes are consistent with the results reported in Bardoux *et al.*, where the piezoelectric field is found to be negligible in InGaN/GaN nanocolumns [123]. In Figs. 4.5(b) and (c), the PL decay traces for the NW ensemble and a sample containing a single InGaN QW are displayed. The decay trace for the

NW ensemble show a double-exponential decay, which has a faster component with a lifetime ~ 400 ps and a slower component with a lifetime ~ 4.3 ns. Since the faster decay lifetime equals roughly to the average value of individual NWs, the faster decay component can be attributed to the recombination of excitons localized in the InGaN localization centers. However, the origin of the slower decay component is not clear yet. A similar double-exponential decay has been reported for InGaN/GaN nanocolumns in Ref. [122]. The slower decay component is likely to arise from the recombination of spatially separated electrons and holes in different localization sites in the InGaN layer. In contrast to NWs, the decay trace for the conventional QW sample shows a stretched exponential with an initial effective lifetime of ~ 20 ns (at which the intensity dropped to $1/e$). The much longer decay lifetime in QW is due to the presence of a strong polarization field, which separates the electrons and holes in the QW and hence reduced the oscillatory strength.

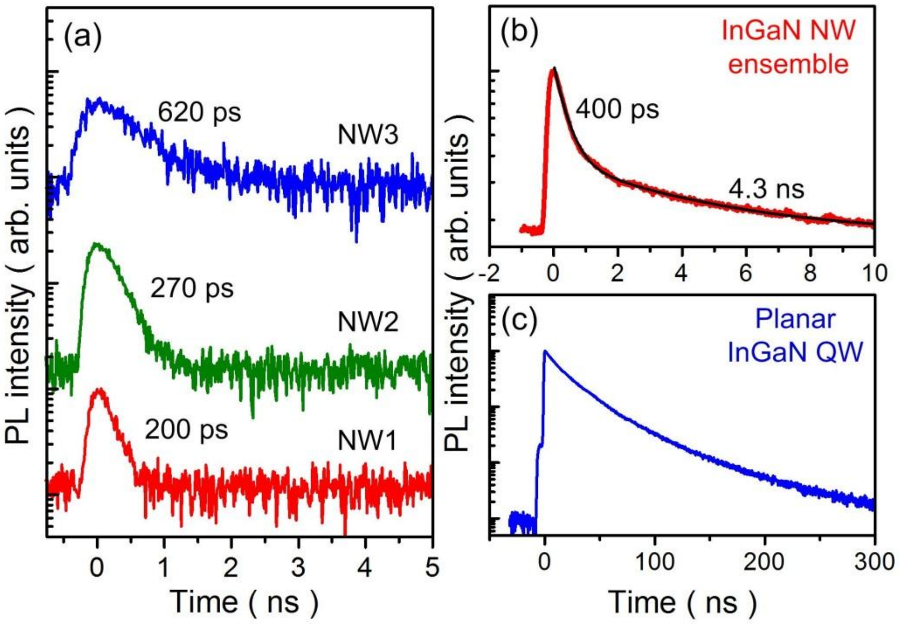

Fig. 4.5: (a) Time-resolved PL traces for localized excitons in three different InGaN/GaN NWs. The decay traces for (b) the NW ensemble and (c) a planar sample containing a single InGaN/GaN QW.

4.2.4 Simulation of strain distribution

According to the experimental results presented above, it is evident that the polarization field in the investigated InGaN/GaN NW heterostructures is *insignificant*. However, recent calculations based FEM for thicker InGaN/GaN NW heterostructures with diameters of 140 nm [125] and ~50 nm [126] revealed that the elastic relaxation through the NW geometry is only marginal. To obtain quantitative values of strain relaxation in thinner NWs investigated here, we have performed FEM simulations for a 2 nm thick $In_{0.1}Ga_{0.9}N$ disk capped by a 5 nm thick GaN layer in a GaN NW with a diameter of 18 nm using a commercially available software. As shown in Fig. 4.6(a), the calculated ε_{xx} distribution in the InGaN disk on the x-z plane is nonuniform, which remains almost fully strained (-0.9 %) at the disk center and decreases gradually toward the NW sidewalls. A polarization field up to 0.9 MV/cm still resides in the center of the disk, as evident from the calculated potential profile along z direction through $x = 0$ shown in Fig. 4.6(b). In a 2 nm $In_{0.1}Ga_{0.9}N$ QW, an internal field up to 0.9 MV/cm can lead to a blueshift of about 12 meV in the transition energy if the internal field was reduced by 20 % due to screening. This suggests that, despite NWs with a diameter of only 18 nm, the strain relaxation via the NW geometry is still inefficient and cannot explain the insignificant polarization induced QCSE.

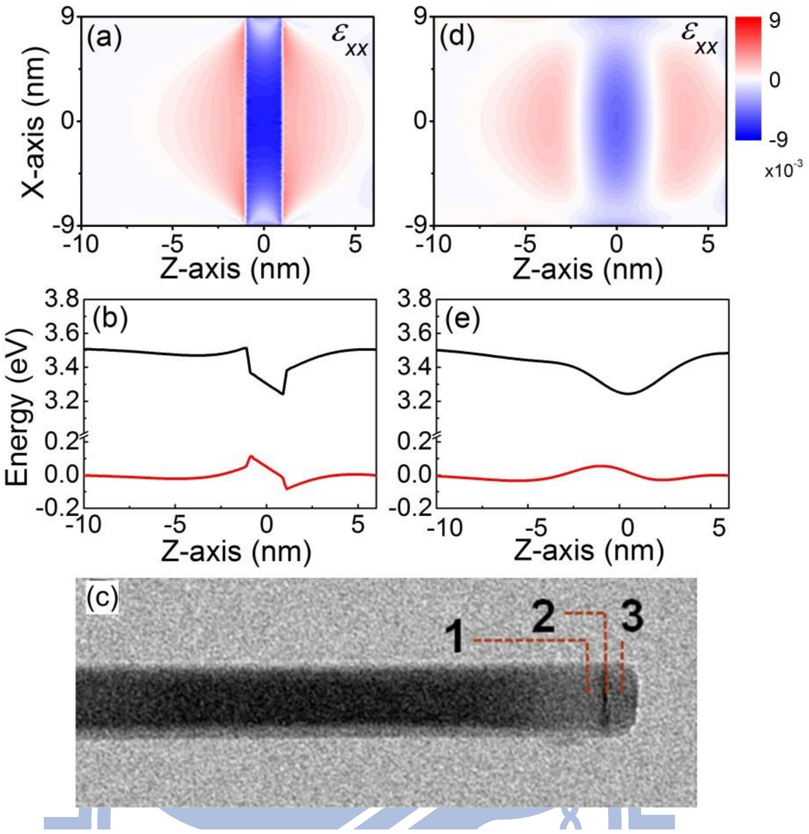

Fig. 4.6 : (a) Calculated strain distribution of $\mathcal{E}_{xx}$ on the *x*-*z* plane and (b) the corresponding band profile along *z* at *x*=0 for an InGaN/GaN NW with a diameter of 18 nm. (c) Composition analysis using STEM-EDX shows that the local In composition are 2.9 %, 10 % and 3.1 % when focusing the electron beam on positions 1, 2 and 3, respectively. (d) and (e) are the same as (a,b), except that the In-Ga intermixing is taken into account.

To account for the insignificant polarization field, we have inspected all the structural analyses for the investigated InGaN/GaN NW heterostructures. From high resolution transmission electron microscopy (HR-TEM) studies, no extended defect was found in the InGaN layer and the vicinal GaN regions. This excludes that strain is released by the formation of dislocations in the InGaN layer. Composition analysis using scanning TEM equipped with energy dispersive X-ray (STEM-EDX) spectroscopy showed that the indium distributions at InGaN-GaN interfaces are not abrupt. This is evident from the STEM-EDX analysis for a NW shown in Fig. 4.6 (c), where the indium composition is found to be 2.9 %, 10 % and 3.1 % when focusing the electron beam on the GaN region (1), the disk layer (2) and the GaN capping layer (3), respectively. Such a composition distribution could arise from In-Ga intermixing during the NW growth, especially when a high growth temperature (750 °C) was used for the InGaN layer and the subsequent GaN capping layer. It has been shown that the QCSE depends sensitively on the interface abruptness of QW structure. Therefore, it is necessary to consider the intermixed composition profile in the FEM simulations. Here, we describe the In distribution by the standard error function profile, which is given by [131,132]

$$c(z)=\frac{c_0}{2}\left[erf\left(\frac{w+2z}{4L_d}\right)+erf\left(\frac{w-2z}{4L_d}\right)\right] \qquad (4.1)$$

where c_0 is the initial In molar fraction before intermixing, w is the disk thickness and $L_d=\sqrt{Dt}$ is the diffusion length. After considering intermixing in FEM simulations, we found that the strain and hence the internal field are reduced considerably, as shown in Fig. 4.6(d) and (e). From the calculated band profile (x = 0) shown in Fig. 4.6(e), the potential at the QW interfaces are softened by the In-Ga intermixing, which can improve the electron-hole wave function overlap and hence reduce the QCSE. This may explain the lack of excitation induced blueshift and the fast recombination lifetimes for the localized emissions from the InGaN/GaN NWs.

In summary, single InGaN/GaN NWs with diameters in the range of 9-27 nm have been investigated by μPL measurements. Sharp emission lines originated from the recombination of localized excitons in the InGaN layer can be resolved at low temperatures. Excitation dependent energy shifts together with spectral diffusions of these emission lines indicated a weak QCSE caused by nearby charged traps, rather than the polarization field in the InGaN/GaN heterostructures. The absence of polarization field is further confirmed by time-resolved PL measurements. Numerical simulations based FEM indicated that strain relaxation via the NW geometry is inadequate and cannot account for the insignificant polarization induced QCSE. Composition analyses STEM-EDX together with FEM simulations suggested that In-Ga intermixing, which softens the abruptness of InGaN/GaN interfaces, may be a possible reason for the insignificant polarization fields in the InGaN/GaN NWs.

4.3 Bandgap tuning of InGaN/GaN nanowires

It is well known that the bandstructure can be affected significantly by the residual strain in the nitride semiconductors. For wurtzite structures, the presence of uniaxial strain will break the C_{6v} crystal symmetry. This leads a splitting between the heavy-hole and light-hole bands [133]. On the other hand, the C_{6v} crystal symmetry is still maintained under biaxial compressive or tensile strain. Therefore, only the crystal field splitting energy can be influenced and observed [134]. The commonly accepted concept for a planar wurtzite structure is that a tensile strain will result in a bandgap decreasing while a compressive strain cause a bandgap increasing. Recently, the presence of relatively non-uniform strain distribution in 1-D nanowire heterostructures as compared with the planar structure has been suggested due to the influence of the reduced symmetry. However, the effects of strain on electronic structure of InGaN/GaN NWs have not been systematically investigated. Therefore, further understanding of the strain field in such 1-D nanowire becomes important since the strain will have the profound effect on the energy bandstructure and the optical properties.

In this section, we studied the strain effects on bandgap energy by applying an external stress using a piezoelectric actuator. The luminescence peak energy of InGaN/GaN NWs shows blueshift with the applied compressive stress. According to numerical simulations, applying a biaxial stress will induce an anisotropic strain along the NW. Due to the lack of internal electric field and quantum confinement effect in NW heterostructures, the shift in the PL peak energy can be attributed to the strain induced change in the energy gap.

4.3.1 Experimental setup for applying stress

For applying the external stress on InGaN/GaN NWs, the deposited NWs were mechanically scratched from the substrate and then dispersed in methanol after the growth. The solution was then dropped onto Si substrate. Therefore, the separated NWs can be obtained on the substrate after drying. Then, the NWs were transferred on a 320 μm piezoelectric actuator $[Pb(Mg_{1/3}Nb_{2/3})O_3]_{0.72}$- $[PbTiO_3]_{0.28}$ (PMN-PT) for applying stress as shown in the Fig. 4.7. Here, the Ti/Ag was coated on the top and rear surfaces as electrodes. A more detailed discussion of PMN-PT can be found in Appendix. To effectively transfer the NWs on to the actuator, a ~ 400 nm superglue was spin coated on the metal and baked at 100 ^{o}C for 3 min. Finally, the prepared Si substrate with NWs was upside down and pressed on to the actuator. After removing the Si substrate, the NWs were firmly glued on the Ag metal. According to the piezoelectric effects of PMN-PT, the external biaxial strain can be induced in the NWs if the out-of-plane electric field is applied across the two electrodes.

For optical characterization of the InGaN/GaN NWs, μPL measurements were carried out at $T \sim 6$ K by using a He-Cd laser as an excitation source. The signals were analyzed by a 0.75 m monochromator and detected by a liquid-nitrogen-cooled CCD camera. Before μPL measurements, the PMN-PT was positively poled at 300 V (corresponding to an electric field of 9.38 kV/cm, which is much larger than the coercive field of the PMN-PT) during the cooling process in order to maintain the poled state. Consequently, the compressive and tensile strain can be obtained respectively at $T \sim 6$ K when the applied voltage $V > 0$ or $V < 0$.

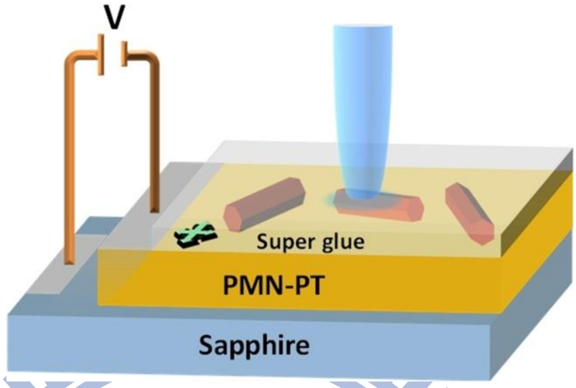

Fig. 4.7 : Schematic illustration of the piezoelectric actuator device used to apply the biaxial stress to the InGaN/GaN NWs.

4.3.2 Photoluminescence spectra under stress

Fig. 4.8 shows the μ-PL spectrum of a single InGaN/GaN NW recorded at 6 K. The emission lines distributed in the range of 3.2-3.4 eV are attributed to the GaN and the lower emission energy with a number of sharp lines in the range of 2.8-3.15 eV belongs to the InGaN quantum disk.

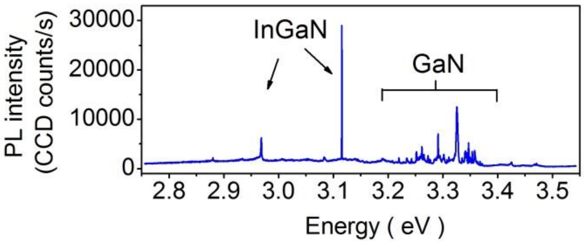

Fig. 4.8: μPL spectrum of single InGaN/GaN NW.

Fig. 4.9 (a) and (b) show the PL intensity map for NWs as a function of the emission wavelength and the applied voltage *V*. A blueshift (redshift) of the emission lines is observed by applying the positive (negative) voltage across the PMN-PT substrate. As mentioned earlier, a compressive in-plane strain can be induced while the positive voltage is applied across the PMN-PT. Therefore, the resulting blueshift (redshift) is observed as the biaxial compressive (tensile) stress is transferred to the 1-D InGaN/GaN NWs.

Besides, we have also observed a difference in energy shift of emission lines with applying voltage as shown in Fig. 4.9 (a) and (b). To further confirm the phenomenon, a statistics of the energy shift rate between *V* = -300 and +500 V from different NWs is shown in Fig. 4.9 (c). In particular, we found that the distribution of energy shift rates can be divided as two regions according to the emission energy. For higher emission energy which is corresponding to the GaN, a higher energy shift rate is observed and it is widespread. On the contrary, the lower and more concentrated energy shift rate is observed in the region of InGaN quantum disk. As we know, the strain induced energy shift in wurtzite III-nitrides can be caused by two effects: the strain-modified bandgap energy and the strain-induced piezoelectric effect. Therefore, the observed distribution of energy shift suggests a nonuniform strain distribution in 1-D NW structures.

Before further discussing the strain distribution in NWs, the external strain provided by PMN-PT should be first estimated through the piezoelectric constant d_{ij} of $PMN_{0.72}$-$PT_{0.28}$. However, the piezoelectric coefficient at low temperature is rarely reported. Here, we used the data reported by Herklotz et al., where the strain at temperatures below 50 K will drop distinctly to about ~1/4 of the room temperature [135]. This temperature evolution of piezoelectric strain is determined by the measurement of the change in the macroscopic sample dimensions. Consequently, the in-plane biaxial strain produced by PMN-PT at 6 K is assumed to be ≈ 0.0625 % under an applied field of $F = 25$ kV/cm.

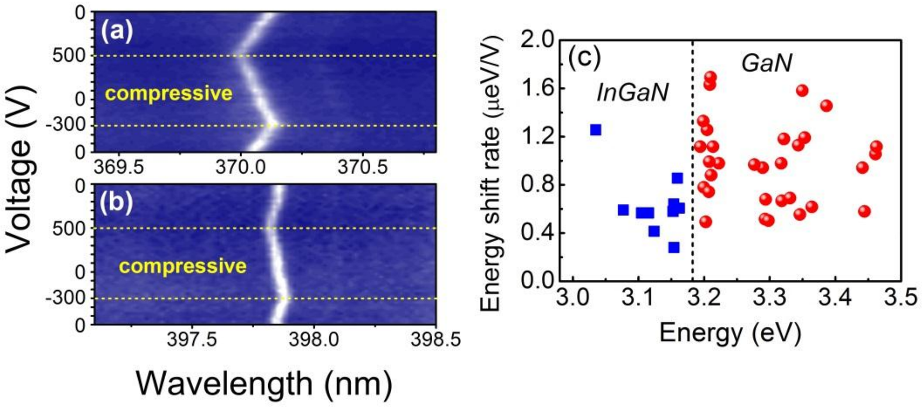

Fig. 4.9: (a) and (b) Color-coded PL intensity map for a NW as a function of the emission wavelength and bias voltage applied to the PMN-PT. (c) A statistics of the energy shift rate between V = -300 and 500 V from different NWs.

4.3.3 Simulation of strain distribution

After estimation of the amount of external strain provided by PMN-PT, we then used the finite-element method (FEM) to simulate the strain distribution in a single NW under the external biaxial stress. All materials are considered as isotropic materials except for the NW. The Young's modulus and Poisson's ratio are listed in Tab. 4.1. For exploring the strain distribution in a NW, the external biaxial compressive stress is applying in the x-z plane of a NW and the simulation results are shown in the Fig. 4.10.

It is obviously indicated that the compressive strain still existed in the z-direction (ε_{zz}). However, the tensile strain existed in the x (ε_{xx}) and y (ε_{yy})-direction even though the external compressive strain applied in the x-direction. The maximum compressive strain of ε_{zz} is -0.060 % and the maximum tensile strain of ε_{xx} (ε_{yy}) is +0.010 % (+0.014 %) in a NW center. This result indicated that the external compressive strain ε_{xx} has been reversed to the tensile strain and the amount of strain is nearly the 1/6 ε_{zz}. In other words, it clearly demonstrated that applying a biaxial stress will induce an anisotropic strain along the NW. Besides, we can also observe that the strain is relatively more dominant at the wire centre than in the region near the wire edge. It is also evident that the nonuniform strain distribution existed in a 1-D NW under the external biaxial stress.

Tab. 4.1: Simulation parameters of Young's modulus and Poisson's ratio.

Material	Young's modulus (GPa)	Possion's ratio
Superglue	9	0.31
Ti	40	0.36
Ag	83	0.37

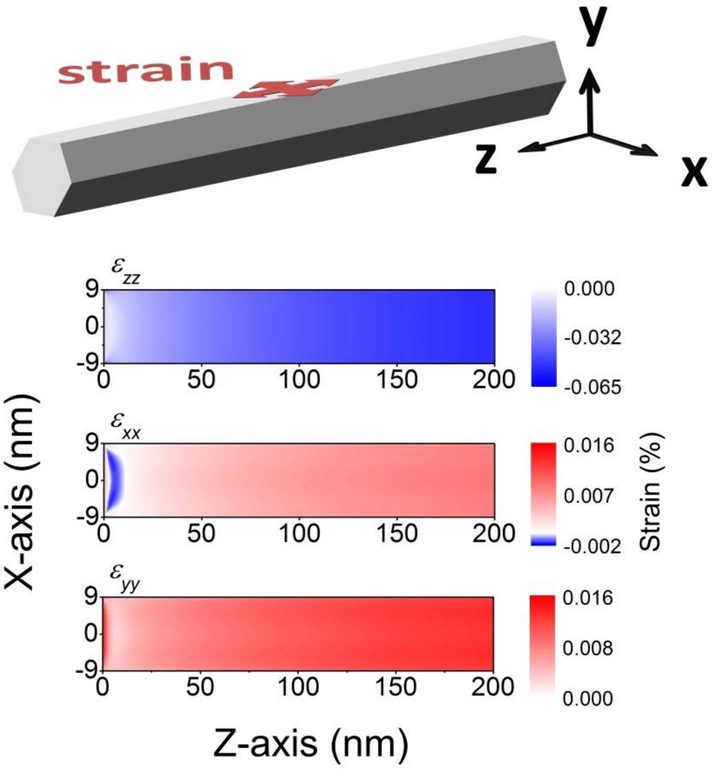

Fig. 4.10: Simulation of strain distribution in a NW under external biaxial compressive stress applied in x-z plane.

After discussing the strain distribution, the energy shift in a single NW can then be determined. As we know, the strain induced piezoelectric field is suppressed in an InGaN/GaN NW, which is evident in an above section. Besides, the lateral quantum confinement effect (x-y plane) can also be neglected because the bohr radius of $In_{0.1}Ga_{0.9}N$ is nearly 3 nm, which is much smaller than the average diameter of InGaN quantum disk (18 nm). Therefore, the experimental observation of energy shift can be attributed to the strain induced change in the energy gap.

For wurtzite structures, the strain-modified bandgap energy is correlated to strains and deformation potentials as follows:

$$\Delta E_c = a_{cz}\varepsilon_{zz} + a_{ct}(\varepsilon_{xx} + \varepsilon_{yy}) \tag{4.2}$$

$$\Delta E_v = (D_1 + D_3)\varepsilon_{zz} + (D_2 + D_4)(\varepsilon_{xx} + \varepsilon_{yy}) \tag{4.3}$$

The a_{ci} and D_i are the conduction band and valence band deformation potentials, respectively. Based on the equations, the bandgap shift can be determined by $\Delta E_g = \Delta E_c - \Delta E_v$. Fig. 4.11 (a) shows the calculated bandgap shift rate in a x-y plane at different positions of a NW. The center of InGaN quantum disk is 6 nm below the wire tip and the wire length is setting as 1 μm. Indeed, it is indicated that the calcuated bandgap shift rate is increasing gradually from the edge to the center of a NW due to the nonuniform strain distribution.

In order to explain the observation of energy shift distribution in NWs in detail, the average energy shift rate in a NW at different position is then calculated from Fig. 4.11 (a). We found that the calculated average energy shift rate is increasing from 1.25 to 3.80 μeV/V as the distance from the wire tip is increasing from 6 to 500 nm [see Fig. 4.11 (b)]. According to the structures of NWs, the most regions of NWs are GaN except for the 5 nm below the wire tip (InGaN quantum disk). Thererfore, the higher and more widespread dsitribution of energy shift rate in GaN than InGaN can be understood and it is also consistent with what we observed from experimental results.

While the observed energy shift with applying external stress is good in considering the nonuniform strain distribution in NWs, the experimental results are only approximately half of the simulation results. Here, two possible causes for the discrepancy are suggested. One is the imperfect fabrication process in piezoelectric actuator device. The other cause may be the uncertainty in the related material constants such as the young’s modulus of superglue. For the small young’s modulus of superglue, the relatively soft layer absorbs much of the strain from PMN-PT and does not transfer it fully to the NW.

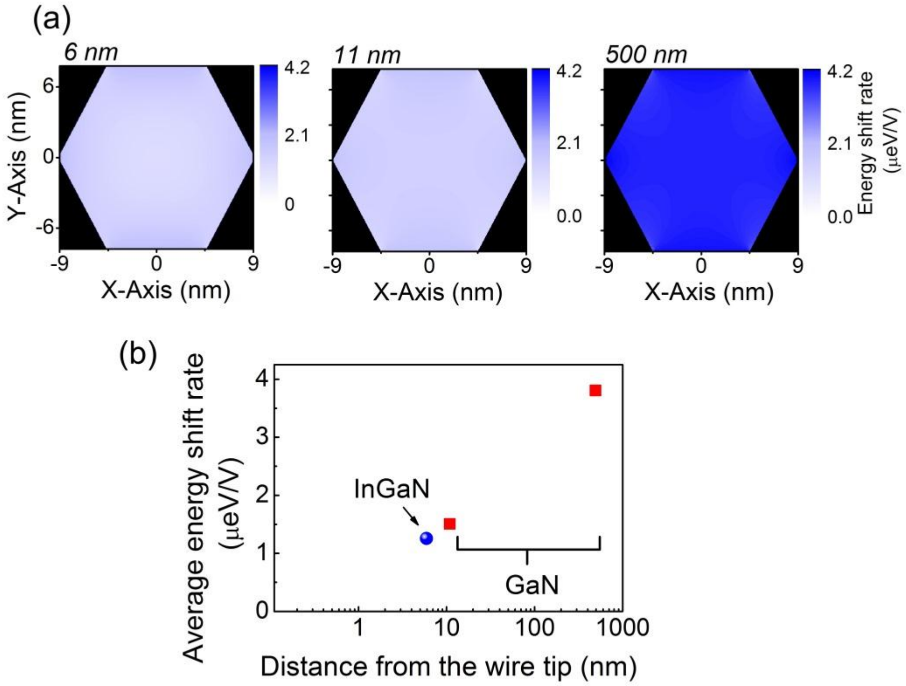

Fig. 4.11: (a) Color-coded maps of bandgap shift rate in x-y plane at different position of a NW. (b) The amount of the average energy shift rate. The center of InGaN quantum disk is 6 nm below the wire tip and the wire length is setting as 1 μm.

In conclusion, we demonstrate the band-gap tuning of InGaN/GaN NW heterostructures by applying an external stress using a piezoelectric actuator. The luminescence peak energy of InGaN/GaN NWs shows blueshift with the applied compressive stress. According to numerical simulations, applying a biaxial stress will induce an anisotropic strain along the NW. Due to the lack of internal electric field and quantum confinement effect in NW heterostructures, the shift in the PL peak energy can be attributed to the strain induced change in the energy gap.

Chapter 5 Conclusions

We have presented the physical features of the $In_xGa_{1-x}N$ nanostructures in many respects based our recent investigations. Here we summarize the conclusions acquired from our structural and optical investigations about the $In_xGa_{1-x}N$ nanostructures as follows.

In the first part of the dissertation, strain relaxation and nucleation process of $In_xGa_{1-x}N$ nanostructures are comprehensively studied. The Raman spectroscopy has been utilized to study the strain relaxation in uncapped InN/GaN islands of different sizes. A redshift in the Raman peak with the island's aspect ratio was observed, regardless of how the InN islands were grown. Most of the initial compressive strain at the InN-GaN interface was found to be released plastically, with a relaxation degree up to > 96 %, during the initial stage of island formations. After that, the residual strain of only -3.5×10^{-3}, was further relaxed elastically via the surface islanding. Based on a simplified 2D model analysis and full 3D simulations, we established the relationship of the strain relaxation in InN/GaN islands with their size and shape. Besides, the surface morphologies, alloy compositions and PL properties of In-rich InGaN nanodots grown by MOCVD at $T_g = 550$-750 °C have also been investigated. The nucleation of InGaN dots was found to be dominated by the surface migration of In adatoms. In particular, we found that the incorporation of Ga into InN during the growth of InGaN dots is governed by adatom migration capability, which tends to decompose into In-rich islands and a thin Ga-rich layer at higher growth temperatures. In-rich islands exhibit PL emission in the NIR range, while the formation of a thin Ga-rich layer is likely to be responsible for the observed visible emission band. After understanding the strain relaxation of InN islands during the initial stage, the strain distribution of Ga-rich InGaN films with different thickness and composition are also discussed. Firstly, the double PL peaks associated with strained and relaxed phase in the InGaN films were clarified. Formation mechanism of two phases with different strain states is also discussed through the RSM. By comparing the RSM and PL results, the correlation between emission energies and two phases were demonstrated. According to the temperature-dependent and time-resolved PL (TRPL), it is indicated that the room temperature PL intensity was dominated by relaxed phase and it has been suggested to highly correlate with the defect densities in InGaN films. Besides, we also demonstrate that the more localization centers existed in relaxed phase than strained one from TRPL measurements. Therefore, we can observe the enhancement of the room-temperature PL intensity of relaxed phase even though the existence of more defect densities.

In the second part of the dissertation, we present the unique characterizations of 1-D InGaN/GaN NWs grown by MBE. The optical properties of single InGaN/GaN NWs with thin diameter distributed in the range of 9-27 nm are investigated. Sharp emission lines originated from the recombination of localized excitons in the InGaN nanodisk layers can be resolved at low temperatures. Excitation dependent energy shifts together with spectral diffusions of these emission lines indicate the presence of a weak QCSE caused by nearby charged traps, rather than the polarization field in the InGaN/GaN heterostructures. The absence of polarization field is further confirmed by time-resolved PL measurements. On the other hand, simulations based on FEM suggest that the strain relaxation via the NW geometry remains marginal even when the NW diameter is reduced to 9 nm. Composition analyses from scanning transmission electron microscopy (STEM) together with numerical simulations suggest that indium interdiffusion may be a possible reason for the absence of piezoelectric polarization fields in the thin InGaN/GaN NWs. After discussing the general features of InGaN/GaN nanowires, bandgap tuning of InGaN/GaN nanowire (NW) heterostructures by applying an external stress using a piezoelectric actuator is also demonstrated. The luminescence peak energy of InGaN/GaN NWs shows blueshift with the applied compressive stress. According to numerical simulations, applying a biaxial stress will induce an anisotropic strain along the NW. Due to the lack of internal electric field and quantum confinement effect in NW heterostructures, the shift in the PL peak energy can be attributed to the strain induced change in the energy gap.

Appendixes

A Material Parameters for $In_xGa_{1-x}N$ Alloy

Tab. A.1: Some important material parameters for InGaN alloy

Parameters	symbol	unit	Values for $In_xGa_{1-x}N$
Lattice constant	a	Å	$3.189+0.3488\,x$
	c	Å	$5.185+0.5183\,x$
Valence band offset	VBO	eV	$0.5\,x$
Conduction band deformation potential	a_{cz}	eV	$-4.9+1.4\,x$
	a_{ct}	eV	$-11.3+7.8\,x$
Valence band deformation potential	D_1	eV	-3.7
	D_2	eV	4.5
	D_3	eV	8.2
	D_4	eV	-4.1
Elastic constant	C_{11}	Gpa	$367-144\,x$
	C_{12}	Gpa	$135-20\,x$
	C_{13}	Gpa	$103-11\,x$
	C_{33}	Gpa	$405-181\,x$
	C_{44}	Gpa	$95-47\,x$
Piezoelectric constant	e_{31}	Cm^{-2}	$-0.32-0.16\,x$
	e_{33}	Cm^{-2}	$0.63+0.42\,x$
	e_{15}	Cm^{-2}	$-0.32+0.58\,x$

B Introduction of PMN-PT

$Pb(Mg_{1/3}Nb_{2/3})O_3]_{(1-x)}$-$[PbTiO_3]_{(x)}$ (PMN-PT) is a new generation of piezoelectric materials. It has a high temperature cubic phase like many ferroelectrics such as $BaTiO_3$ and $PbTiO_3$ etc. The cubic phase is centrosymmetric and therefore is paraelectric. It will become ferroelectric after undergoing a structural phase transition upon cooling and poling process. The unite cells of the paraelectric cubic phase and the ferroelectric tetragonal phase can be seen in Fig. B.1.

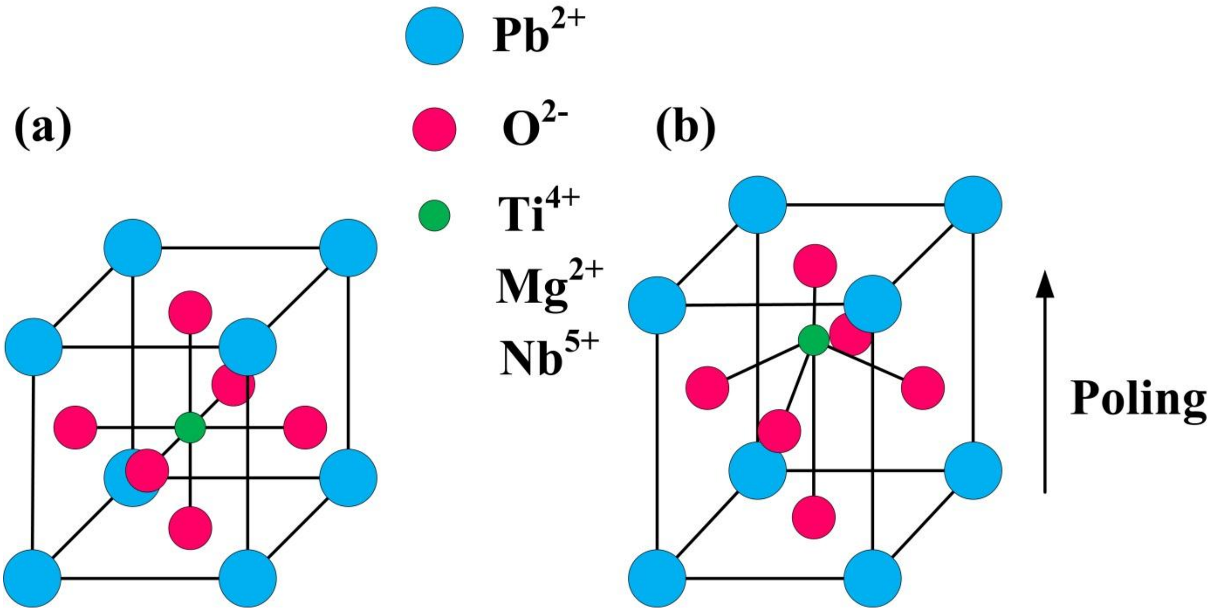

Fig. B.1: Unit cells of PMN-PT. (a) Paraelectric cubic phase and (b) ferroelectric phase under cooling and polling.

A structural transformation from the cubic phase to the tetragonal (T), rhombohedral (R) or orthorhombic (O) phases can result in a spontaneous polarization in <001>, <111> or <110> direction respectively. It is mainly associated with shape and volume changes of the cubic structure. The shape change (strain) is typically an elongation along the polarization direction and a contraction in the plane perpendicular to the polarization direction.

As we know, the strain which is produced by PMN-PT can be estimated from the electric field and the piezoelectric coefficient d_{ij} ($\varepsilon = E \cdot d_{ij}$). However, the piezoelectric coefficients vary apparently in different crystal orientation as shown in Tab. B.2. Therefore, the external stress can be applied in the uniaxial-like or biaxial types by careful choosing the crystal orientations of PMN-PT.

Tab. B.2: Piezoelectric coefficients d_{ij} of PMN-0.28PT

	d_{31} (pC/N)	d_{32} (pC/N)	d_{33}(pC/N)
PMN-0.28PT [001]	-1000	-1000	2000
PMN-0.28PT [011]	723	-1761	1766

In summary, the PMN-PT has been found to exhibit high piezoelectric coefficient, large electric-mechanical coupling coefficient, high dielectric constants and low dielectric losses.

1896

Therefore, it is a good candidate material in various sensor, actuator, and transducer applications.

1896

Reference

1. S. Nakamura, T. Mukai, and M, Senoh, Appl. Phys. Lett. **64**,1687 (1994).
2. S. Nakamura, M. Senoh, N. Iwasa, S. I. Nagahama, T. Yamada, T. Mukai, Jpn. J. Appl. Phys. **34**, L1332 (1995).
3. S. Nakamura, M. Senoh, S. Nagahama, N. Iwasa, T. Yamada, T. Matsushita, H. Kiyoku, and Y. Sugimoto, Jpn. J. Appl. Phys., Part 2 **35**, L74 (1996).
4. K. Itaya, M. Onomura, J. Nishino, L. Sugiura, S. Saito, M. Suzuki, J. Rennie, S. Nunoue, M. Yamamoto, H. Fujimoto, Y. Kokubun, Y. Ohba, G. Hatakoshi, and M. Ishikawa, Jpn. J. Appl. Phys., Part 2 **35**, L1315 (1996).
5. K. Itaya, M. Onomura, J. Nishino, L. Sugiura, S. Saito, M. Suzuki, J. Rennie, S. Nunoue, M. Yamamoto, H. Fujimoto, Y. Kokubun, Y. Ohba, G. Hatakoshi, and M. Ishikawa, Jpn. J. Appl. Phys., Part 2 **35**, L1315 (1996).
6. F. M. Steranka *et al*, Phys. Status Solidi a **194**, 380 (2002).
7. S. Chichibu, T. Azuhata, T. Sota, and S. Nakamura, Appl. Phys. Lett. **69**, 4188 (1996).
8. C. Kisielowski, Z. Liliental-Weber, and S. Nakamura, Jpn. J. Appl. Phys., Part 1 **36**, 6932 (1997).
9. Y. Narukawa, Y. Kawakami, M. Funato, S. Fujita, S. Fujita, and S. Nakamura, Appl. Phys. Lett. **70**, 981 (1997).
10. K. P. O'Donnell, R. W. Martin, and P. G. Middleton, Phys. Rev. Lett. **82**, 237 (1999).
11. T. M. Smeeton, M. J. Kappers, J. S. Barnard, M. E. Vickers, and C. J. Humphreys, Appl. Phys. Lett. **84**, 4110 (2004).
12. S. Pereira, M. R. Correia, E. Pereira, C. Trager-Cowan, F. Sweeney, K. P. O'Donnell, E. Alves, N. Franco, and A. D. Sequeira, Appl. Phys. Lett. **81**, 1207 (2002).
13. A. Hangleiter, F. Hitzel, C. Netzel, D. Fuhrmann, U. Rossow, G. Ade, and P. Hinze, Phys. Rev. Lett. **95**, 127402 (2005)
14. T. Takeuchi, S. Sota, M. Katsuragawa, M. Komori, H. Takeuchi, H. Amano, and I. Akasaki, Jpn. J. Appl. Phys., Part 2 **36**, L382 (1997).
15. T. Bretagnon, P. Lefebvre, P. Valvin, R. Bardoux, T. Guillet, T. Taliercio, B. Gil, N. Grandjean, F. Semond, B. Damilano, A. Dussaigne, and J. Massies, Phys. Rev. B **73**, 113304 (2006).

16. S. F. Chichibu, A. C. Abare, M. P. Mack, M. S. Minsky, T. Deguchi, D. Cohen, P. Kozodoy, S. B. Fleischer, S. Keller, J. S. Speck, J. E. Bowers, E. Hu, U. K. Mishra, L. A. Coldren, S. P. Denbaars, K. Wada, T. Sota, and S. Nakamura, Mater. Sci. Eng. B **59**, 298 (1999).

17. J. Wu, W. Walukiewicz, K. M. Yu, J. W. Ager III, E. E. Haller, H. Lu, W. J. Schaff, Y. Saito, and Y. Nanishi, Appl. Phys. Lett. **80**, 3967 (2002).

18. T. Matsuoka, H. Okamoto, M. Nakao, H. Harima, and E. Kurimoto, Appl. Phys. Lett. **81**, 1246 (2002).

19. M. Hori, K. Kano, T. Yamaguchi, Y. Saito, T. Araki, Y. Nanishi, N. Teraguchi, and A. Suzuki, Phys. Status Solidi B **234**, 750 (2002).

20. V. Y. Davydov, A. A. Klochikhin, V. V. Emtsev, D. A. Kurdyukov, S. V. Ivanov, V. A. Vekshin, F. Bechstedt, J. Furthmüller, J. Aderhold, J. Graul, A. V. Mudryi, H. Harima, A. Hashimoto, A. Yamamoto and E. E. Haller, Phys. Status Solidi B **234**, 787 (2002).

21. Y. Saito, H. Harima, E. Kurimoto, T. Yamaguchi, N. Teraguchi, A. Suzuki, T. Araki, and Y. Nanishi, Phys. Status Solidi B **234**, 796 (2002).

22. L. Hsu, and W. Walukiewicz, J. Appl. Phys. **104**, 024507 (2008).

23. M. Asada, Y. Miyamoto, and Y. Suematsu, IEEE J. Quantum Electron. **22**, 1915 (1986).

24. Y. Arakawa, and H, Sakaki, Appl. Phys. Lett. **40**, 939 (1982).

25. M. S. Hu, W. M. Wang, T. T. Chen, L. S. Hong, C. W. Chen, C. C. Chen, Y. F. Chen, K. H. Chen, L. C. Chen, Adv. Funct. Mater. **16**, 537 (2006).

26. S. C. Shi, C. F. Chen, G. M. Hsu, J. S. Hwang, S. Chattopadhyay, Z. H. Lan, K. H. Chen, L. C. Chen, Appl. Phys. Lett. **87**, 203103 (2005).

27. I. Ho and G. B. Stringfellow, Appl. Phys. Lett. **69**, 2701 (1996).

28. R. Singh, D. Doppalapudi, T. D. Moustakas, and L. T. Romano, Appl.

Phys. Lett. **70**, 1089 (1997).

29. N. A. El-Masry, E. L. Piner, S. X. Liu, and S. M. Bedair, Appl. Phys. Lett. **72**, 40 (1998).

30. S. Y. Karpov, MRS Internet J. Nitride Semicond. Res. **3**, 16 (1998).

31. A. Tabata, L. K. Teles, L. M. R. Scolfaro, J. R. Leite, A. Kharchenko, T. Frey, D. J. As, D. Schikora, K. Lischka, J. Furthmüller, and F. Bechstedt, Appl. Phys. Lett. **80**, 769 (2002).

32. A. Yamamoto, Y. Nakagawa, T. Sugiura, and A. Hashimoto, Phys. Status Solidi A **176**,

237 (1999).

33. E. Iliopoulos, A. Georgakilas, E. Dimakis, A. Adikimenakis, K. Tsagaraki, M. Androulidaki, and N. T. Pelekanos, Phys. Status Solidi A **203**, 102 (2006).

34. T. Kuykendall, P. Ulrich, S. Aloni, and P. Yang, Nature Mater. **6**, 951 (2007).

35. V. Yu. Davydov, A. A. Klochikhin, V. V. Emtsev, S. V. Ivanov, V. V. Vekshin F. Bechstedt, J. Furthmüller, H. Harima, A. V. Mudryi, A. Hashimoto, A.Yamamoto, J. Aderhold, J. Graul, and E. E. Haller, phys. stat. sol. (b) **230**, R4 (2002).

36. J. Wu, W. Walukiewicz, K. M. Yu, J. W. Ager III, E. E. Haller, H. Lu, and W. J. Schaff, Appl. Phys. Lett. **80**, 4741 (2002).

37. Y. Nanishi, Y. Saito, and T. Yamaguchi, Jpn. J. Appl. Phys. 42, 2549 (2003).

38. P. Laukkanen, S. Lehkonen, P. Uusimaa, M. Pessa, A. Sepala, T. Ahlgren, E. Rauhala, J. Cryst. Growth **230**, 503 (2001).

39. C. A. Chang, C. F. Shih, N. C. Chen, T. Y. Lin, and K. S. Liu, Appl. Phys. Lett. **85**, 6131 (2004).

40. B. N. Pantha, J. Li, J. Y. Lin, and H. X. Jiang, Appl. Phys. Lett. **93**, 182107 (2008).

41. V. Yu. Davydov, N. S. Averkiev, I. N. Goncharuk, D. K. Nelson, I. P. Nikitina, A. S. Polkovnikov, A. N. Smirnov, M. A. Jacobson, and O. K. Semchinova, J. Appl. Phys. **82**, 5097 (1997).

42. T. Kozawa, T. Kachi, H. Kano, H. Nagase, N. Koide, and K. Manabe, J. Appl. Phys. **77**, 4389 (1995).

43. C. Kisielowski, J. Krüger, S. Ruvimov, T. Suski, J. W. Ager, III, E. Jones, Z. Liliental-Weber, M. Rubin, E. R. Weber , M. D. Bremser and R. F. Davis, Phys. Rev. B **54**, 17745 (1996).

44. H.-J. Kwon, Y.-H. Lee, O. Miki, H. Yamano, and A. Yoshida, Appl. Phys. Lett. **69**, 937 (1996).

45. W. K. Chen, H. C. Lin, Y. C. Pan, J. Ou, C. K. Shu, W. H. Chen, and M. C. Lee, Jpn. J. Appl. Phys., Part 1 **37**, 4870 (1998).

46. J. S. Dyck, K. Kash, K. Kim, W. R. L. Lambrecht, C. C. Hayman, A. Argoitia, M. T. Grossner, W. L. Zhou, and J. C. Angus, Mater. Res. Soc. Symp. Proc. **482**, 549 (1998).

47. G. Kaczmarczyk *et al.*, Appl. Phys. Lett. **76**, 2122 (2000).

48. X. Wang, S. B. Che, Y. Ishitani, and A. Yoshikawa, Appl. Phys. Lett. **89**, 171907 (2006).

49. C. Pinquier, F. Demangeot, J. Frandon, J. W. Pomeroy, M. Kuball, H. Hubel, N. W. A. van Uden, D. J. Dunstan, O. Briot, B. Maleyre, S. Ruffenach, and B. Gil, Phys. Rev. B **70**, 113202 (2004).

50. J. W. Chen, Y. F. Chen, H. Lu, and W. J. Schaff, Appl. Phys. Lett. **87**, 041907 (2005).

51. X. Wang, S. B. Che, Y. Ishitani, and A. Yoshikawa, J. Appl. Phys. **99**, 073512 (2006).

52. V. S. Harutyunyan, P. Specht, J. Ho, and E. B. Weber, Defect Diffus. Forum **226-228**, 79 (2004).

53. A. F. Wright, J. Appl. Phys. **82**, 2833 (1997).

54. K. Kim, W. R. L. Lambrecht, and B. Segall, Phys. Rev. B **53**, 16310 (1996).

55. S. Yu. Davydov, Semiconductors **36**, 41 (2002).

56. F. Bernardini, V. Fiorentini, and D. Vanderbilt, Phys. Rev. B **56**, R10024 (1997).

57. K. Shimada, T. Sota and K. Suzuki J. Appl. Phys. **84** 4951 (1998).

58. A. Al-Yacoub, and L. Bellaiche, Appl. Phys. Lett. **79** 2166 (2001).

59. F. Bernardini, and V. Fiorentini, Appl. Phys. Lett. **80** 4145 (2002).

60. S. Muensit, and I. L. Guy Appl. Phys. Lett. **72** 1896 (1998).

61. A. Hangleiter, F. Hitzel, S. Lahmann and U. Rossow, Appl. Phys. Lett. **83** 1169 (2003).

62. I. L. Guy, S. Muensit, and E. M. Goldys, Appl. Phys. Lett. **75**, 4133 (1999).

63. D. Doppalapudi, S. N. Basu, K. F. Ludwig, and T. D. Moustakas, J. Appl. Phys. **84**, 1389 (1998).

64. A. Wakahara, T. Tokuda, X-Z. Dang, S. Noda, and A. Sasaki, Appl. Phys. Lett. **71**, 906 (1997).

65. M. Rao, D. Kim, and S. Mahajan, Appl. Phys. Lett. **85**, 1961 (2004).

66. Z. Liliental-Weber, D. N. Zakharov, K. M. Yu, J. W. Ager III, W. Walukiewicz, E. E. Haller, H. Lu, and W. J. Schott, J. Electron Microsc. **54**, 243 (2005).

67. S. Hernández, R. Cuscó, D. Pastor, L. Artús, K. P. O'Donnell, R. W. Martin, I. M. Watson, Y. Nanishi, and E. Calleja, J. Appl. Phys. **98**, 013511 (2005).

68. T. Stoica, R. J. Meijers, R. Calarco, T. Richter, E. Sutter, and H. Luth, Nano Lett. **6**, 1541

(2006).

69. Y. G. Cao, M. H. Xie, Y. Liu, Y. F. Ng, H. S. Wu, and S. Y. Tong, Appl. Phys. Lett. **83**, 5157 (2003).

70. Y. E. Romanyuk, R.-G. Dengel1, L. V. Stebounova, and S. R. Leone, J. Cryst. Growth **304**, 346 (2007).

71. C.-H. Shen, H.-W. Lin, H.-M. Lee, C.-L. Wu, J.-T. Hsu, and S. Gwo, Thin Solid Films **494**, 79 (2006).

72. W. C. Ke, C. P. Fu, C. Y. Chen, L. Lee, C. S. Ku, W. C. Chou, W.-H. Chang, M. C. Lee, W. K. Chen, W. J. Lin, and Y. C. Cheng, Appl. Phys. Lett. **88**, 191913 (2006).

73. A. F. Jarjour, R. A. Oliver, A. Tahraoui, M. J. Kappers, C. J. Humphreys, and R. A. Taylor, Phys. Rev. Lett. **99**, 197403 (2007).

74. Y. F. Ng, Y. G. Cao, M. H. Xie, X. L. Xie, X. L. Wang, and S. Y. Tong, Appl. Phys. Lett. **81**, 3960 (2002).

75. J. G. Lozano, A. M. Sanchez, R. Garcia, D. Gonzalez, O. Briot and S. Ruffenach, Appl. Phys. Lett. **88**, 151913 (2006).

76. F. Demangeot, J. Frandon, C. Pinquier, M. Caumont, O. Briot, B. Maleyre, S. Clur-Ruffenach, and B. Gil, Phys. Rev. B **68**, 245308 (2003).

77. I. Ho and G. B. Stringfellow, Appl. Phys. Lett. **69**, 2701 (1996).

78. A. Kahchner, A. Hoffmann, C. Thomsen, T. Bottcher, S. Einfeldt, and D. Hommel, Phys. Status. Solidi a **179**, R4 (2000)

79. E. Silveira, A. Tabata, J. R. Leite, R. Trentin, V. Lemos, T. Frey, D. J. As, D. Schikora, and K. Lischka, Appl. Phys. Lett. **75**, 3602 (1999).

80. S. Nakamura, Science **281**, 956 (1998).

81. H. Hirayama, S. Tanaka, P. Ramvall, and Y. Aoyagi, Appl. Phys. Lett. **72**, 1736 (1998).

82. K. Tachibana, T. Someya, and Y. Arakawa, Appl. Phys. Lett. **74**, 383 (1999).

83. B. Damilano, N. Grandjean, S. Dalmasso, and J. Massies, Appl. Phys. Lett. **75**, 3751 (1999).

84. C. Adelmann, J. Simon, G. Feuillet, N. T. Pelekanos, B. Daudin, and G. Fishman, Appl. Phys. Lett. **76**, 1570 (2000).

85. W. C. Ke, L. Lee, C. Y. Chen, W. C. Tsai, W.-H. Chang, W. C. Chou, M. C. Lee, W. K.

Chen, W. J. Lin, and Y. C. Cheng, Appl. Phys. Lett. **89**, 263117 (2006).

86. H. Lu, W. J. Schaff, J. Hwang, H. Wu, W. Yeo, A. Pharkya, and L. F. Eastman, Appl. Phys. Lett. **77**, 2548 (2000).

87. R. S. Qhalid Fareed, R. Jain, R. Gaska, M. S. Shur, J. Wu, W. Walukiewicz, and M. Asif Khan, Appl. Phys. Lett. **84**, 1892 (2004).

88. J. G. Lozano, A. M. Sánchez, R. García, D. González, M. Herrera, N. D. Browning, S. Ruffenach and O. Briot, Appl. Phys. Lett. **91**, 071915 (2007).

89. R. Kern and P. Müller, Surf. Sci. **392**, 103 (1997).

90. V. Lebedev, V. Cimalla, J. Pezoldt, M. Himmerlich, S. Krischok, J. A. Schaefer, O. Ambacher, F. M. Morales, J. G. Lozano and D. Gonzalez, J. Appl. Phys. **100**, 094902 (2006).

91. The 3D strain simulation is performed using the finite-element package COMSOL Multiphysics® .

92. E. F. Schubert and J. K. Kim "Solid-state light sources getting smart," Science **308**, 1274-1278 (2005).

93. P. Kung, M. Razegui, Opto-Electron. Rev. **8**, 201 (2000).

94. Y. Li, J. Xiang, F. Qian, S. Gradecak, Y. Wu, H. Yan, D. A. Blom, and C. M. Lieber, Nano Lett. **6**, 1468 (2006).

95. J. Wu, W. Walukiewicz, K. M. Yu, W. Shan, J. W. Ager, E. E. Haller, Hai Lu, William J. Schaff, W. K. Metzger, and Sarah Kurtz, J. Appl. Phys. **94**, 6477 (2003).

96. O. Jani, I. Ferguson, C. Honsberg, and S. Kurtz, Appl. Phys. Lett. **91**,132117 (2007).

97. R. Dahal, B. Pantha, J. Li, J. Y. Lin, and H. X. Jiang, Appl. Phys. Lett. **94**, 063505 (2009).

98. S. Pereira, M. R. Correia, E. Pereira, K. P. O'Donnell, E. Alves, A. D. Sequeira, N. Franco, I. M. Watson, and C. J. Deatcher, Appl. Phys. Lett. **80**, 3913 (2002).

99. A. Kar, D. Alexson, M. Dutta, and M. A. Stroscio, J. Appl. Phys. **104**, 073502 (2008).

100. For a review, see, for example, A. G. Bhuiyan, A. Hashimoto, and A. Yamamoto, J. Appl. Phys. **94**,2779 (2003).

101. C. A. Chang, T, Y. Tang, P. H. Chang, N. C. Chen, and C. T. Liang, Jpn. J. Appl. Phys. **46**, 2840 (2007).

102. B. N. Pantha, J. Li, J. Y. Lin, and H. X. Jiang, Appl. Phys. Lett. **96**, 232105 (2010).

103. S. Chichibu, K. Wada, and S. Nakamura, Appl. Phys. Lett. **71**, 2346 (1997).

104. Y.-T. Moon, D.-J. Kim, J.-S. Park, J.-T. Oh, J.-M. Lee, Y.-W. Ok, H. Kim, and S.-J. Park, Appl. Phys. Lett. **79**, 599 (2001).

105. T. Detchprohm, K. Hiramatsu, K. Itoh, and I. Akasaki, Jpn. J. Appl. Phys., Part 2 **31**, L1454 (1992).

106. W. Paszkowicz, Powder Diffr. **14**, 258 (1999).

107. K. Hiramatsu, Y. Kawaguchi, M. Shimizu, N. Sawaki, T. Zheleva, R. Davis, H. Tsuda, W. Taki, N. Kuwano, K. Oki, MRS Internet J. Nitride Semicond. Res. **2**, 6 (1997).

108. S. F. Chichibu, T. Onuma, T. Aoyama, K. Nakajima, P. Ahmet, T. Chikyow, T. Sota, S. P. Denbaars, S. Nakamura, T. Kitamura, Y. Ishida, and H. Okumura, J. Vac. Sci. Technol. B **21,** 1856 (2003).

109. H. T. Grahn, *Introduction to Semiconductor Physics* (World Scientific, Singapore, 1999).

110. E. D. Minot, F. Kelkensberg, M. van Kouwen, J. A. van Dam, L. P. Kouwenhoven, V. Zwiller, M. T. Borgstrom, O. Wunnicke, M. A. Verheijen, and E. P. A. M. Bakkers, Nano Lett. **7**, 367 (2007)

111. M. T. Borgstrom, V. Zwiller, E. Muller, and A. Imamoglu, Nano Lett. **5**, 1439 (2005)

112. Y. Gu, E. S. Kwak, J. L. Lensch, J. E. Allen, T. W. Odom, and L. J. Lauhon, Appl. Phys. Lett. **87**, 043111 (2005).

113. D. Wallin, A. Fuhrer, L. E. Froberg, L. Samuelson, H. Q. Xu, S. Hofling, and A. Forchel, Appl. Phys. Lett. **90**, 172112 (2007)

114. S. Nakamura and S. F. Chichibu, *Introduction to Nitride Semiconductor Blue Laser and Light Emitting Diodes* (Taylor & Francis, London, 2000).

115. H. Morkoc, Handbook of Nitride Semiconductors and Devices, Vols. I-III (Wiley, New York, 2008).

116. A. Kikuchi, M. Kawai, M. Tada, and K. Kishino, Jpn. J. Appl. Phys. **43**, L1524 (2004).

117. C. –C. Hong, H. Ahn, C. –Y. Wu, and S. Gwo, Opt. Express **17**, 17227 (2009).

118. Y. –L. Chang, J. L. Wang, F. Li, and Z. Mi, Appl. Phys. Lett. **96**, 013106 (2010).

119. H. -W. Lin, Y. J. Lu, H. Y. Chen, H. M. Lee, and S. Gwo, Appl. Phys. Lett. **97**, 073101 (2010).

120. R. Armitage and K. Tsubaki, Nanotechnology **21**,195202 (2010).

121. H. P. T. Nguyen, S. Zhang, K. Cui, X. Han, S. Fathololoumi, M. Couillard, G. A. Botton, and Z. Mi, Nano Lett. **11**,1919 (2011)

122. Y. Kawakami, S. Suzuki, A. Kaneta, M. Funato, A. Kikuchi, and K. Kishino, Appl. Phys. Lett. 89, 163124 (2006).

123. R. Bardoux, A. Kaneta, M. Funato, Y. Kawakami, A. Kikuchi, and K. Kishino, Phys. Rev. B **79**, 155307 (2009)

124. M. J. Holmes, Y. S. Park, J. H. Warner, and R. A. Taylor, Appl. Phys. Lett. **95**, 181910 (2009).

125. M. J. Holmes, Y. S. Park, X. Wang, C. C. S. Chan, A. F. Jarjour, R. A. Taylor, J. H. Warner, J. Luo, H. A. R. El-Ella, and R. A. Oliver, J. Appl. Phys. **109**, 063515 (2011).

126. M. Knelangen, M. Hanke, E. Luna, L. Schrottke, O. Brandt, and A. Trampert, Nanotechnology 22, 365703 (2011).

127. J. Lahneman, O. Brandt, C. Pfuller, T. Flissikowski, U. Jahn, E. Luna, M. Hanke, M. Knelangen, A. Trampert, and H. T. Grahn, Phys. Rev. B 84, 155303 (2011)

128. Y. T. Chen, W. C. Tsai, W. Y. Chen, C. L. Hsiao, H. C. Hsu, W. –H. Chang, T. M. Hsu, K. H. Chen, and L. C. Chen, Opt. Express **20**, (2012).

129. H. Schomig, S. Halm, A. Forchel, G. Bacher, J. Off, and F. Scholz, Phys. Rev. Lett. **92**, 106802 (2004).

130. O. Moriwaki, T. Someya, K. Tachibana, S. Ishida, and Y, Arakawa, Appl. Phys. Lett. **76**, 2361 (2000).

131. M. C. Y. Chan, C. Surya, and P. K. A. Wai, J. Appl. Phys. **90**, 197 (2001).

132. C. –C. Chen, T. –H. Hsueh, Y. –S. Ting, G. –C. Chi, and C. –A. Chang, J. Appl. Phys. **90**, 5180 (2001).

133. Q. Yan, P. Rinke, M. Winkelnkemper, A. Qteish, D. Bimberg, M. Scheffler, and C. G. Van de Walle, Semicond. Sci. Technol. **26**, 014037, (2011).

134. M. Suzuki, and T. Uenoy, Jpn. J. Appl. Phys. **35**, 1420, 1996.

135. A. Herklotz, J. D. Plumhof, A. Rastelli, O. G. Schmidt, L. Schultz, and K. Dorr, J. Appl. Phys. **108**, 094101 (2010).

Publication Lists

A. Publications

1. Y. T. Chen, **W. C. Tsai**, W. Y. Chen, C. L. Hsiao, H. C. Hsu, W. –H. Chang, T. M. *Hsu*, K. H. Chen, and L. C. Chen, *” *Growth of sparse arrays of narrow GaN nanorods hosting spectrally stable InGaN quantum disks”*, Opt. Express **20**, 16166 (2012).

2. F. W. Huang, J. K. Sheu,* S. J. Tu, P. C. Chen, Y. H. Yeh, M. L. Lee, W. C. Lai, **W. C. Tsai**, and W. –H. Chang, *"Optical properties of Mn in regrown GaN-based epitaxial layers "*, Opt. Mater. Express **2**, 469 (2012).

3. F. W. Huang, J. K. Sheu,* M. L. Lee, S. J. Tu, W. C. Lai, **W. C. Tsai**, and W. –H. Chang *"Linear photon up-conversion of 450 meV in InGaN/GaN multiple quantum wells via Mn-doped GaN intermediate band photodetection "*, Opt. Express **19**, A1211 (2011).

4. **W. C. Tsai**, F. Y. Lin, W. C. Ke, S. K. Lu, S. J. Cheng, W. C. Chou, W. K. Chen, M. C. Lee and W. H. Chang*, *"Size-dependent strain relaxation in InN islands grown on GaN by metalorganic chemical vapor deposition"* , Appl. Phys. Lett. **94**, 063102 (2009).

5. S. F. Fu, S. M. Wang, Ling Lee, C. Y. Chen, **W. C. Tsai**, W. C. Chou, M. C. Lee, W. H. Chang, and W. K. Chen*, “*The structural and optical properties of InN nanodots grown with various V/III ratios by metal-organic chemical vapor deposition*” Nanotechnology **20**, 295702 (2009).

6. W. -H. Chang*, W. C. Ke, L. Lee, C. Y. Chen, **W. C. Tsai**, H. Lin, W. C. Chou, W. K. Chen and M. C. Lee, *"Effects of Growth Temperature on InN/GaN Nanodots Grown by Metalorganic Chemical Vapor Deposition"* , J. Appl. Phys. **103**, 104306 (2008),

7. **W. C. Tsai**, H. Lin, W. C. Ke, W. -H. Chang*, W. C. Chou, W. K. Chen and M. C. Lee, *"Structural and optical properties of In-rich InGaN nanodots grown by metalorganic chemical vapor deposition"* , Nanotechnology **18**, 405305 (2007).

8. W. C. Ke, L. Lee, C. Y. Chen, **W. C. Tsai**, W. –H. Chang, W. C. Chou, M. C. Lee, and W. K. Chen*, “*Impacts of ammonia background flows on structural and photoluminescence properties of InN dots grown on GaN by flow-rate modulation epitaxy”* Appl. Phys. Lett. **89**, 263117 (2006).

9. W. C. Ke, C. P. Fu, C. C. Huang, C. S. Ku, L. Lee, C. Y. Chen, **W. C. Tsai**, W. K. Chen*, M. C. Lee, W. C. Chou, W. J. Lin, Y. C. Cheng, "*Optical properties and carrier dynamics of self-assembled* $GaN/Al_{0.11}Ga_{0.89}N$ *quantum dots*" Nanotechnology **17**, 2609 (2006).

B. International Conference Reports

1. **W. C. Tsai**, H. Lin, W. C. Ke, W.-H. Chang*, W. C. Chou, W. K. Chen and M. C. Lee, *"Structural and Optical Properties of Indium-Rich InGaN Islands"* , Phys. Stat. Sol.(c) 5, 1702 (2008).
2. W. -H. Chang*, L. Lee, C. Y. Chen, **W. C. Tsai**, H. Lin, W. C. Chou, W. K. Chen, M. C. Lee, *"Structural and Optical Properties of InN/GaN Islands Grown by Metalorganic Chemical Vapor Deposition"* , Phys. Stat. Sol. (c) 5, 3014 (2008).